Forcing microbubbles in microfluidics

Irene de Arcos González Turmo

The work in this thesis was carried out at Dpto. Ingeniería Aeroespacial y Mecánica de Fluidos of Escuela Técnica Superior de Ingeniería, Universidad de Sevilla. It is part of the research programme "Tecnologías micro- y nanofluídicas facilitadoras esenciales para aplicaciones biomédicas, biotecnológicas y de salud pública", which is financially supported by the Spanish Government Ministry MEIC (DPI2013-46485).

Publisher:
Irene Arcos-Turmo, Dpto. Ingeniería Aeroespacial y Mecánica de Fluidos, Escuela Técnica Superior de Ingeniería, Universidad de Sevilla,
Camino de los Descubrimientos s/n, CP 41007 Sevilla, Spain

FORCING MICROBUBBLES IN MICROFLUIDICS

THESIS

to obtain
the degree of doctor at the Universidad de Sevilla,
on the authority of the Rector Magnificus,
Prof. Dr. Miguel. Á. Castro Arroyo,
according to the decision of the
Doctorate Board to defend in public
on Tuesday 11st June 2019

by

Irene de Arcos González Turmo
born on 3rd October 1990
in Sevilla

This thesis has been approved by the supervisors:

Prof. Dr. Alfonso M. Gañán Calvo

and

Associate Prof. Dr. Elena de Castro Hernández

Bubbles are your goal but also your worst enemy.
Keep them under control!

Contents

1 Introduction

The present thesis deals with microbubbles subject to external forces, such as an acoustic excitation or a forced liquid flow. In most cases, the external force is applied to enhance microbubble generation in terms of stability, microbubble size, production frequency, or to gain active control on any of these characteristics. In other cases, as in pinned bubbles, the external force, such as an acoustic excitation, aims to control the surrounding liquid flow, the bubble interface or even to force the ejection of new microbubbles by cavitation.

Due to the current diversity of microbubble applications, the present thesis main motivation is to obtain a better comprehension of the role that these external forces have. The improvement in microbubble generation due to an external force can have a direct and considerable impact in a number of different fields, such as medicine, biology, new materials or food industry, to name some of them. Nonetheless, the applicability of microbubbles on those fields will depend on the bubble characteristics: size distribution, polydispersity, involved fluids, generation frequency or even shape.

1.1 Microbubbles applications

Among all microbubbles applications, the use of bubbles as contrast agent for ultrasound imaging and other therapeutic applications might be considered the golden key of the moment (van der Meer et al, 2007; Castro-Hernández et al, 2011; Tang

et al, 2011; Callens et al, 2015). Here, microbubbles are subject to an acoustic field -generally ultrasonic-, which results in an induced non-inertial cavitation. The number of scientific works published on this subject has been increasing during the last decade without sign of saturation. Typically covered by a lipid coating to transport and release certain medicines and/or avoid their dissolution, bubbles are injected into the bloodstream to enhance medical ultrasound imaging contrast. When irradiated with an ultrasound pulse, bubbles experience volumetric oscillations that reemit ultrasound waves back to the transducer, improving the image contrast. Frequencies of the bubble natural frequency, which depend on the bubble size, are selected to enhance the process. Thus, monodisperse bubbles are desired for this application. Likewise bubbles smaller than blood vessels and of the order of red blood cells, between $2\,\mu$m and $5\,\mu$m, are required to avoid embolisms. Once inside the blood stream, bubbles can be optically or acoustically triggered by means of lasers or ultrasound waves to blast them and release their substances. Other medical or therapeutical applications for microbubbles are sonoporation (enhancing the drug uptake by oscillating microbubbles nearby cells) (Rinaldi et al, 2018), sonothrombolysis (Brown et al, 2011) or oxygen carrier (Leonard, 2003).

Apart from the latter non-inertial cavitation, inertial bubble cavitation, in which the bubble rapidly collapses creating a shock wave, are also employed in medicine. High intensity focused ultrasound (HIFU) is, for instance, a cancer treatment surgery in which long ultrasonic pulses create a thermal ablation in the deep tissues (Khokhlova et al, 2011). These inertially cavitated microbubbles are been also employed for cleaning purposes, as in ultrasonic baths and Cavitation Intensifying Bags (CIBs) (Verhaagen and Rivas, 2016; van Zwieten et al, 2017) or in chemical engineering for water purification or sonochemical reactions (Rivas et al, 2013).

With completely different characteristics in terms of size and distribution to the ones employed in ultrasound imaging, bubbles are also widely used for water aeration in DAF (Dissolved Air Flotation) and IAF (Induced Air Flotation) processes during sewage treatment (Kim et al, 2015), water aeration for algae or fish farming (Zimmerman et al, 2009) or for drag reduction on ships (Kumagai et al, 2015; Verschoof et al, 2016). Here, polydisperse and larger microbubbles -even macrobubbles- are desired, between $80\,\mu$m and 5 mm depending on their purpose.

The food industry is another rising field in microbubbles uses, with a combination of bubble characteristics from the two previously mentioned applications. Encouraged by multinational companies, bubbles are used to diminish fat content, create new textures or increase organoleptic properties, such as the creamy mouthfeel in oily or dietary products (Gañán-Calvo, 2001; Erni et al, 2009; Rovers et al, 2015, 2016). As an example, the use of monodisperse microbubbles in foams leads to a better stability,

i.e time with optimum properties (Ganan-Calvo et al, 2004). Both, monodisperse or polydisperse microbubbles with sizes varying between microns and few millimeters are demanded at generally high production rates.

Additionally, new materials, in which bubbles are introduced to decrease weight or cost (Fernández et al, 2008; Testouri et al, 2012), are been developed. Hollow metallic spheres are produced to be used as hollow semiconductor or organometallic particles (Wan, 2012), to name an example.

However, microbubbles applications are not only restricted to the need of mass-producing them. Indeed, rather than generating bubbles, several applications are based on the use of bubbles attached to different surfaces or devices. The progressive understanding of microbubbles physics and their performance when subjected to different external processes, such as electrical (Di Bari and Robinson, 2013; Van Der Linde et al, 2017) and -specially relevant- acoustic/mechanical excitation (Marmottant and Hilgenfeldt, 2004; Gelderblom et al, 2012), has broadened microbubble applications. Fluid motion control (Bolaños-Jiménez et al, 2017), mixing or microswimming (Bertin et al, 2015) are some examples of the latter. Here, the precise control of the interface is what generates the desired output.

Regarding the fluids employed in the previously described applications, microbubbles were initially generated in Newtonian liquids, such as water, glycerol or acetone (Ganán-Calvo and Gordillo, 2001; Garstecki et al, 2006), and later on for biological purposes in liquids such as blood, plasma or similars (Bento et al, 2017). In ultrasound imaging, coatings such as lipids, phospholipids, polymers, particles, proteins as well as different gases: perfluorocarbon or octafluoropropane are used. In the recent decades, microbubbles for the production of new materials has broadened their study to non-newtonian fluids, specially polymers (Studart et al, 2006; Quell et al, 2015; Laborie et al, 2016).

1.2 Microdevices and working regimes

The pursuit of small, narrowly-distributed and controllable microbubbles, while simultaneously mass-produced, has broken into the research on microfluidic devices, as an attractive method capable of producing the characteristics needed in most of the applications described in the previous section. Nowadays, microbubbles generation methods have diverged from the membrane filters, agitation or sonication procedures initially (but still) employed in the industrial mass-production of bubbles. Although simple and cheap, these initial procedures have a poor control on bubble diameter and size distribution. The ultrasonic bath based on sonication techniques, or the use

of membrane filters for fish and algae farming and sewage treatment might be some examples of the latter. If non-exhaustive bubble size control but high production rates are required, as it could sometimes be the case in, for instance, sewage treatment or food industry, these procedures might still be used. However, microfluidic devices are chosen if their benefits in terms of bubble diameter and size distribution control want to be acquired.

Microfluidics devices, where liquid and gas flows converge to form microbubbles, have characteristic channel dimensions between micrometers or hundredth of micrometers and can be implemented in axisymmetric and planar configuration. A wide range of devices have been developed in the last three decades (Garstecki et al, 2005; Rodríguez-Rodríguez et al, 2015). Flow focusing, -both planar (Gordillo et al, 2004; Garstecki et al, 2004) and axisymmetric (Ganán-Calvo and Gordillo, 2001)-, T-junctions (Garstecki et al, 2006; Dollet et al, 2008), and cross-junctions (Castro-Hernández et al, 2011) are those with the strongest boost.

Axisymmetric geometries imply three-dimensional designs by means of concentric capillary tubes, as it is the case of the well-known axisymmetric flow focusing. Here, a focusing effect is added by forcing both, liquid and gas flows, through a small constriction or aperture of diameter D. The axisymmetric flow focusing device is characterized by the exit channel length L and the distance between the gas inlet and the exit channel, H. On the other hand, planar configurations take advantage of techniques like micromachining or the popular and low-cost soft lithography (PDMS), which allows the direct visualization of the flow and an easier production. T-Junction, cross-junction, and planar flow focusing are commonly implemented in soft lithography. Nevertheless, combinations of the three-dimensional devices properties and planar mass-production methods are been also explored during the last years (Castro-Hernandez et al, 2016; Zhang et al, 2014).

Among these microfluidics devices, three global regimes can be identified: (i) a squeezing regime, where bubbles are formed at the entrance of the outlet channel by blocking it, (ii) a jetting regime, characterized by the generation of a jet that breaks up into bubbles, and (iii) a bubbling regime, where bubbles are formed from a cone-like shape at low production rates. Each regime characterizes a microfluidic device and displays its optimal performance under a combination of geometry and working conditions. Figure 1.1 shows these four main devices, which are now further described.

T-junctions are simple but robust devices, working in squeezing regime. The gas flow plugs the exit diameter and the bubble is generated once the liquid pressure rises enough and overcomes the gas blockage. The pinch-off process in this regime

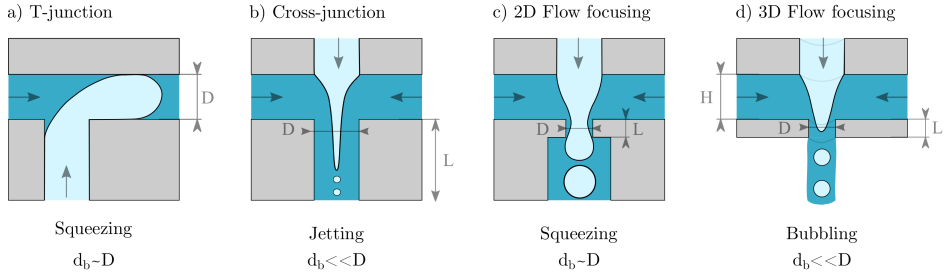

Figure 1.1: Most popular microfluidic devices, including their working regimes and characteristic bubble size d_b: a) T-junction, b) cross-junction, c) planar flow focusing and d) axisymmetric flow focusing. Dark blue denotes liquid and light blue gas.

commonly results in bubble diameters of the order of the device exit diameter D.

Cross-junctions allow the formation of bubbles considerably smaller than the characteristic geometric length due to its jetting condition. Here, the length of the exit channel, L, is much longer than the exit diameter D, $L \sim 10D$, stabilizing the first milliseconds of the generated bubble trail. A steady tapering gas meniscus arises, from which bubbles are ejected, thus ensuring the production of monodisperse microbubbles at high and controlled production scales. The meniscus can be further stabilized by forcing the gas to follow a preferential path, for example, controlling the wetting conditions of the channel or by etching a relief at the entrance of the exit channel.

Planar flow focusing devices, on the contrary, have an exit channel with a length L of the same order than the its diameter D, $L \sim D$. The exit channel also tends to be narrower than the inlet channels width. This constriction forces the device to work in a squeezing regime, where bubbles block the exit channel before being formed.

Last but not least, **axisymmetric flow focusing**, the originator of the planar flow focusing device, tends to create a bubbling regime. At the end of the gas feeding channel, an attached gas cusp, which size and form depend on the surface tension, is formed and a steady short ligament rises due to the focusing liquid flow. Monodisperse bubbles at high production rates are formed. This bubbling regime can be distinguished from the jetting regime by the jet length, which reaches 2 or 3 times the jet diameter in the jetting regime. Nonetheless, the air meniscus can be further stabilized to allow the device to work in jetting conditions and thus, reducing the achievable bubble size, as is accomplished with the Swirl flow focusing device introduced in the present thesis.

Concerning their advantages and drawbacks, the different microdevices reported here are in some way restricted in terms of the achievable absolute flow rates, although the use of planar lithography aims to reduce this limitation. Monodispersity is a common advantage, and those devices working in squeezing regime ,T-junctions and planar flow focusing, show a noteworthy low PDI. Nevertheless, these devices are

limited to lower generation frequencies and higher bubble diameters compared to those working in the jetting regime, such as cross-junctions, with same geometrical dimensions. Last but not least, clogging is one of the most critical factors, limiting liquids and achievable bubble sizes. Thus, due to the need of lower channel dimensions for a desired bubble size, squeezing regime working devices suffer more clogging problems than devices operating in the jetting regime.

References

Bento D, Sousa L, Yaginuma T, Garcia V, Lima R, Miranda JM (2017) Microbubble moving in blood flow in microchannels: effect on the cell-free layer and cell local concentration. Biomedical microdevices 19(1):6

Bertin N, Spelman TA, Stephan O, Gredy L, Bouriau M, Lauga E, Marmottant P (2015) Propulsion of bubble-based acoustic microswimmers. Physical Review Applied 4(6):064012

Bolaños-Jiménez R, Rossi M, Rivas DF, Kähler CJ, Marin A (2017) Streaming flow by oscillating bubbles: quantitative diagnostics via particle tracking velocimetry. Journal of fluid mechanics 820:529–548

Brown AT, Flores R, Hamilton E, Roberson PK, Borrelli MJ, Culp WC (2011) Microbubbles improve sonothrombolysis in vitro and decrease hemorrhage in vivo in a rabbit stroke model. Investigative radiology 46(3)

Callens M, Verboven E, Van Den Abeele K (2015) Investigation of microbubble composition on ultrasonic dispersion properties for biosensing applications. Physics Procedia 70:1237–1240

Castro-Hernández E, van Hoeve W, Lohse D, Gordillo JM (2011) Microbubble generation in a co-flow device operated in a new regime. Lab on a Chip 11(12):2023–2029

Castro-Hernandez E, Kok MP, Versluis M, Rivas DF (2016) Study of the geometry in a 3d flow-focusing device. Microfluidics and nanofluidics 20(2):40

Di Bari S, Robinson AJ (2013) Adiabatic bubble growth in uniform dc electric fields. Experimental Thermal and Fluid Science 44:114–123

Dollet B, Van Hoeve W, Raven JP, Marmottant P, Versluis M (2008) Role of the channel geometry on the bubble pinch-off in flow-focusing devices. Physical review letters 100(3):034504

Erni P, Windhab EJ, Fischer P (2009) Interfacial rheology in food science and technology. In: Interfacial rheology, vol 1, Brill, pp 615–653

Fernández P, Cruz L, Coleto J (2008) Procesos de fabricación de metales celulares. parte i: Procesos por vía líquida. Revista de Metalurgia 44(6):540–555

Gañán-Calvo AM (2001) Enhanced food products. US Patent 6,248,378

Ganan-Calvo AM, Fernandez J, Marquez Oliver A, Marquez M (2004) Coarsening of monodisperse wet microfoams. Applied physics letters 84(24):4989–4991

Ganán-Calvo AM, Gordillo JM (2001) Perfectly monodisperse microbubbling by capillary flow focusing. Physical review letters 87(27):274501

Garstecki P, Gitlin I, DiLuzio W, Whitesides GM, Kumacheva E, Stone HA (2004) Formation of monodisperse bubbles in a microfluidic flow-focusing device. Applied Physics Letters 85(13):2649–2651

Garstecki P, Ganan-Calvo AM, Whitesides G (2005) Formation of bubbles and droplets in microfluidic systems. Technical sciences 53(4)

Garstecki P, Fuerstman MJ, Stone HA, Whitesides GM (2006) Formation of droplets and bubbles in a microfluidic t-junctionñscaling and mechanism of break-up. Lab on a Chip 6(3):437–446

Gelderblom H, Zijlstra AG, van Wijngaarden L, Prosperetti A (2012) Oscillations of a gas pocket on a liquid-covered solid surface. Physics of fluids 24(12):122101

Gordillo JM, Cheng Z, Ganan-Calvo AM, Marquez M, Weitz D (2004) A new device for the generation of microbubbles. Physics of Fluids 16(8):2828–2834

Khokhlova TD, Canney MS, Khokhlova VA, Sapozhnikov OA, Crum LA, Bailey MR (2011) Controlled tissue emulsification produced by high intensity focused ultrasound shock waves and millisecond boiling. The Journal of the Acoustical Society of America 130(5):3498–3510

Kim SJ, Choi J, Jeon YT, Lee Ic, Won CH, Chung J (2015) Microbubble-inducing characteristics depending on various nozzle and pressure in dissolved air flotation process. KSCE Journal of Civil Engineering 19(3):558–563

Kumagai I, Takahashi Y, Murai Y (2015) Power-saving device for air bubble generation using a hydrofoil to reduce ship drag: theory, experiments, and application to ships. Ocean Engineering 95:183–194

Laborie B, Rouyer F, Angelescu DE, Lorenceau E (2016) Yield-stress fluids foams: flow patterns and controlled production in t-junction and flow-focusing devices. Soft matter 12(46):9355–9363

Leonard RJ (2003) The transition from the bubble oxygenator to the microporous membrane oxygenator. Perfusion 18(3):179–183

Marmottant P, Hilgenfeldt S (2004) A bubble-driven microfluidic transport element for bioengineering. Proceedings of the National Academy of Sciences 101(26):9523–9527

van der Meer SM, Dollet B, Voormolen MM, Chin CT, Bouakaz A, de Jong N, Versluis M, Lohse D (2007) Microbubble spectroscopy of ultrasound contrast agents. The Journal of the Acoustical Society of America 121(1):648–656

Quell A, Elsing J, Drenckhan W, Stubenrauch C (2015) Monodisperse polystyrene foams via microfluidics–a novel templating route. Advanced Engineering Materials 17(5):604–609

Rinaldi L, Folliero V, Palomba L, Zannella C, Isticato R, Di Francia R, Berretta M, de Sio I, Adinolfi LE, Morelli G, et al (2018) Sonoporation by microbubbles as gene therapy approach against liver cancer. Oncotarget 9(63):32182

Rivas DF, Stricker L, Zijlstra AG, Gardeniers HJ, Lohse D, Prosperetti A (2013) Ultrasound artificially nucleated bubbles and their sonochemical radical production. Ultrasonics sonochemistry 20(1):510–524

Rodríguez-Rodríguez J, Sevilla A, Martínez-Bazán C, Gordillo JM (2015) Generation of microbubbles with applications to industry and medicine. Annual Review of Fluid Mechanics 47:405–429

Rovers TA, Sala G, Van Der Linden E, Meinders MB (2015) Effect of temperature and pressure on the stability of protein microbubbles. ACS applied materials & interfaces 8(1):333–340

Rovers TA, Sala G, Van der Linden E, Meinders MB (2016) Potential of microbubbles as fat replacer: Effect on rheological, tribological and sensorial properties of model food systems. Journal of Texture Studies 47(3):220–230

Studart AR, Gonzenbach UT, Tervoort E, Gauckler LJ (2006) Processing routes to macroporous ceramics: a review. Journal of the American Ceramic Society 89(6):1771–1789

Tang MX, Loughran J, Stride E, Zhang D, Eckersley RJ (2011) Effect of bubble shell nonlinearity on ultrasound nonlinear propagation through microbubble populations. The Journal of the Acoustical Society of America 129(3):EL76–EL82

Testouri A, Arriaga L, Honorez C, Ranft M, Rodrigues J, van der Net A, Lecchi A, Salonen A, Rio E, Guillermic RM, et al (2012) Generation of porous solids

with well-controlled morphologies by combining foaming and flow chemistry on a lab-on-a-chip. Colloids and Surfaces A: Physicochemical and Engineering Aspects 413:17–24

Van Der Linde P, Moreno Soto Á, Peñas-López P, Rodríguez-Rodríguez J, Lohse D, Gardeniers H, Van Der Meer D, Fernández Rivas D (2017) Electrolysis-driven and pressure-controlled diffusive growth of successive bubbles on microstructured surfaces. Langmuir 33(45):12873–12886

Verhaagen B, Rivas DF (2016) Measuring cavitation and its cleaning effect. Ultrasonics sonochemistry 29:619–628

Verschoof RA, Van Der Veen RC, Sun C, Lohse D (2016) Bubble drag reduction requires large bubbles. Physical review letters 117(10):104502

Wan J (2012) Microfluidic-based synthesis of hydrogel particles for cell microencapsulation and cell-based drug delivery. Polymers 4(2):1084–1108

Zhang JM, Li EQ, Thoroddsen ST (2014) A co-flow-focusing monodisperse microbubble generator. Journal of Micromechanics and Microengineering 24(3):035008

Zimmerman WB, Hewakandamby BN, Tesař V, Bandulasena HH, Omotowa OA (2009) On the design and simulation of an airlift loop bioreactor with microbubble generation by fluidic oscillation. Food and Bioproducts Processing 87(3):215–227

van Zwieten R, Verhaagen B, Schroën K, Rivas DF (2017) Emulsification in novel ultrasonic cavitation intensifying bag reactors. Ultrasonics sonochemistry 36:446–453

2

Novel swirl flow-focusing microfluidic device for the production of monodisperse microbubbles*

A novel swirl flow-focusing microfluidic axisymmetric device for the generation of monodisperse microbubbles at high production rates to be used as in-line contrast agents for medical applications is presented. The swirl effect is induced upstream of the discharge orifice by a circular array of microblades which form a given angle with the radial direction. The induced vortical component on the focusing liquid stabilizes the gas meniscus by the vorticity amplification due to vortex stretching as the liquid is forced through the discharge orifice. The stabilized meniscus tapers into a steady gas ligament that breaks into monodisperse microbubbles. A reduction up to 57% in the microbubble diameter is accomplished when compared to conventional axisymmetric flow-focusing microdevices. An exhaustive experimental study is performed for various blade angles and numerous gas to liquid flow rate ratios, validating previous VoF numerical simulations. The microbubbles issued from the stabilized menisci verify prior scaling law of flow-focusing.

*Published as: Irene Arcos-Turmo, Miguel Ángel Herrada, José María López-Herrera, David Fernandez Rivas, Alfonso M. Gañán-Calvo, and Elena Castro-Hernández. "Novel swirl flow-focusing microfluidic device for the production of monodisperse microbubbles." Microfluidics and Nanofluidics 22, no. 8 (2018): 79

2.1 Introduction

Microbubbles represent not only the obvious counterpart of sprays to diffuse a fluid phase enclosed by surface tension into the environment. Here, the environment is a liquid. Given its enormous inertia combined with high surface tension forces at small scales, the generation, manipulation and dynamics of microbubbles possess unique features not found in any other system. The behavior of microbubbles is often counterintuitive, and generally nonlinear (Marmottant et al, 2005).Thus, the physics involved is drastically dominated by very large inertia effects of the environment and the compressibility of the microbubbles. That compressibility combined with their surface properties make them perfect devices for some critical tasks: in biomedical applications, as contrast agents, or as vehicles for drug delivery, or gene therapy by sonoporation (Takahashi, 2005; Ferrara et al, 2007).

As a proxy to qualify the importance of microbubbles as established devices or tools in medicine, one may compare the relative percentages of scientific articles published mentioning certain combinations of keywords. For example, one may use public databases to assess that the percentage of papers mentioning "ultrasound", and "microbubbl*" or "micro-bubbl*" over the total has stabilized around 0.024% over the last ten years. The vast majority of them use the ultrasound-microbubble coupled dynamics as the key device to produce benefits in "cardio*" or "cancer*" related applications (Wei et al, 1998; Kennedy et al, 2004). For example, this is comparable to the weight of "amiodarone", the most widely used antiarrhythmic drug, in cardiology publications (0.05% of papers over the last five years), which illustrates the social and economic importance of microbubble-contrast agents in certain medical fields. In this regard, one may verify that the number of papers mentioning "cardio*" and "cancer*" have stabilized at 3.5% and 6.8%, respectively, over the last hundred years, making them the highest concerns of medicine since long ago. For applications in these fields as contrast agents, to achieve the highest possible efficiency and to minimize gas infusion and adverse effects, reducing the microbubble size and its dispersion as much as possible is of paramount importance: a focused, single frequency excitation is the best way to manipulate swarms of microbubbles in a liquid (generally, blood) stream.

Thus, the search of physical principles and development of technologies to produce the highest possible surface (or minimum microbubble size) per unit input energy, concentrated around a single size value (monodispersity), has fueled an immense collective effort. Almost unfailingly, the solutions proposed for the efficient one-step generation of microbubbles make use of microfluidic designs. In general terms, microfluidics has co-evolved driven by strong expectations in the areas of biomedicine and new materials (Whitesides, 2006). Here, microfluidic devices have demonstrated to be an attractive method to mass-produce narrowly distributed micron size microbubbles in a wide range of liquids (Gañán-Calvo and Gordillo, 2001; Anna et al, 2003; Garstecki et al, 2006). Several microfluidic techniques have been developed in the last

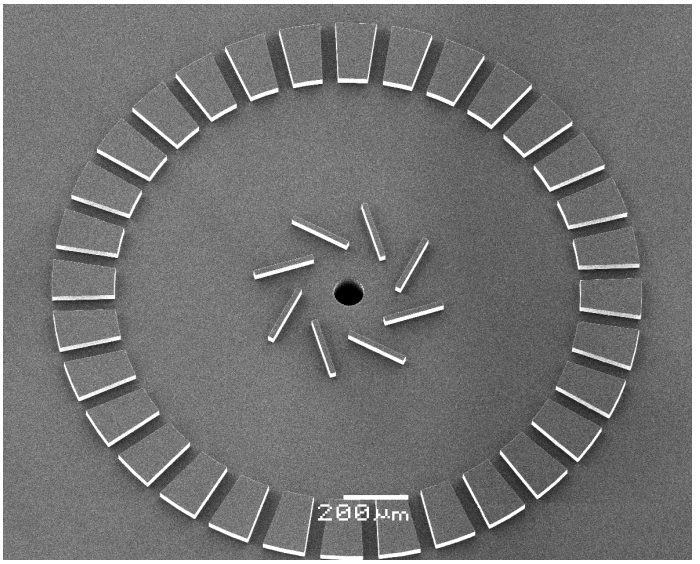

Figure 2.1: SEM image of the 60° blade swirl flow-focusing microfluidic device.

decade, being the T junctions, cross junctions and flow-focusing designs those with the strongest boost.

Despite their differences, two global regimes can be identified: (i) a bubbling regime, where bubbles are formed right at the tip of the injection tube (axisymmetric case) or at the entrance of the outlet channel (planar case), and (ii) a jetting regime characterized by the generation of a jet that breaks up into bubbles (Gañán-Calvo and Gordillo, 2001; Gañán-Calvo, 2004; Gañán-Calvo et al, 2006). These designs can be implemented in axisymmetric geometries (Gañán-Calvo and Gordillo, 2001), by means of concentric capillary tubes, or in planar configurations using techniques such as soft lithography or micromachining. Bubbles generated by planar flow-focusing devices (Garstecki et al, 2004, 2005) and T junctions (Garstecki et al, 2006; Dollet et al, 2008) have usually diameters of the order of the device geometry as a result of the pinch-off process of either the bubbling or squeezing regimes. It is by forcing both, the liquid and gas streams, through a small aperture or constriction, using flow-focusing (Gañán-Calvo and Gordillo, 2001) or cross junctions (Castro-Hernández et al, 2011), that it is possible to achieve bubbles whose size is considerable smaller than the characteristic geometric length. Flow-focusing ensures the production of monodisperse microbubbles at high and controlled production scales. The strong focusing effect created at the constriction induces the formation of a steady tapering gas meniscus, from which bubbles are ejected.
In this work, we propose a robust one-step method to controllably produce small

monodisperse microbubbles in an aqueous liquid stream at high production rate, to be employed -among other uses- as contrast agents for medical applications: a novel swirl flow-focusing (SFF) microfluidic device. The essential geometrical difference of our device with respect to all previous implementations is the presence of a circular blade array, concentric to the exit channel, that forces the liquid to swirl around the exit hole (see Figure 2.1). The centrifugal forces created by the swirl originate an intense pressure gradient in the radial direction, stabilizing the gas meniscus and focusing the gas into a short steady gas ligament. Thus, the imposed swirl enables the formation of a tapering meniscus for a wider range of working experimental conditions than in common flow-focusing. This extends the robustness and versatility of co-flow designs to mass produce very small microbubbles to inaccessible parametrical ranges to other known configurations.

2.2 Materials and methods

2.2.1 Microfluidic chip design and fabrication

The SFF microfluidic device creates the swirl effect by forcing the liquid through a circular blade array, concentric to the exit channel and tangent to the liquid flow. Although the microchip design is 3D, the fabrication process is not. Basically, it consists in a regular 2D engraving into one of the microfluidic chip slabs. Two concentric $50\,\mu$m filters were placed prior to the blade array to homogenize and filter the liquid flow and to reinforce the rigidity of the chip structure. Based on the numerical results obtained using 3D CFD simulations (FLUENT) the following blade parameters were selected: the closest radial position of the blades to the exit channel $R1 = 150\,\mu$m, the blade length $L = 200\,\mu$m, its width $W = 20\,\mu$m, the number of blades $n = 8$ and the pith angle $\alpha = 0^\circ$, 40°, 60° and 80°. Rectangular blades were chosen for fabrication simplicity. The blades height was equal to the height of the chamber $H = 30\,\mu$m.

The device is made up of a glass wafer (100 mm diameter, 1.2 mm thickness, Borofloat 33; Schott Germany) containing the outlet hole and a silicon wafer (p-type, 5-10 Ohm cm resistivity, 100 mm diameter, $525\,\mu$m thickness, $\{100\}$ crystal orientation; Okmetic Finland) which has both, the gas and the liquid inlet holes, and the microfluidic chamber as shown in Figure 2.2.
The $L = 1.2$ mm thick Borofloat glass wafer was processed by FEMTOprint SA (Switzerland) using their 3D microstructuring technique to create a hole with a diameter $D = 80\,\mu$m, throughout the entire thickness of the glass wafer assuring a perfect alignment between the gas inlet and the emulsion outlet. The use of glass has a double purpose: (i) since L/D=15, it serves as a microbubble collection channel and (ii) it allows the transversal view of the exit channel.

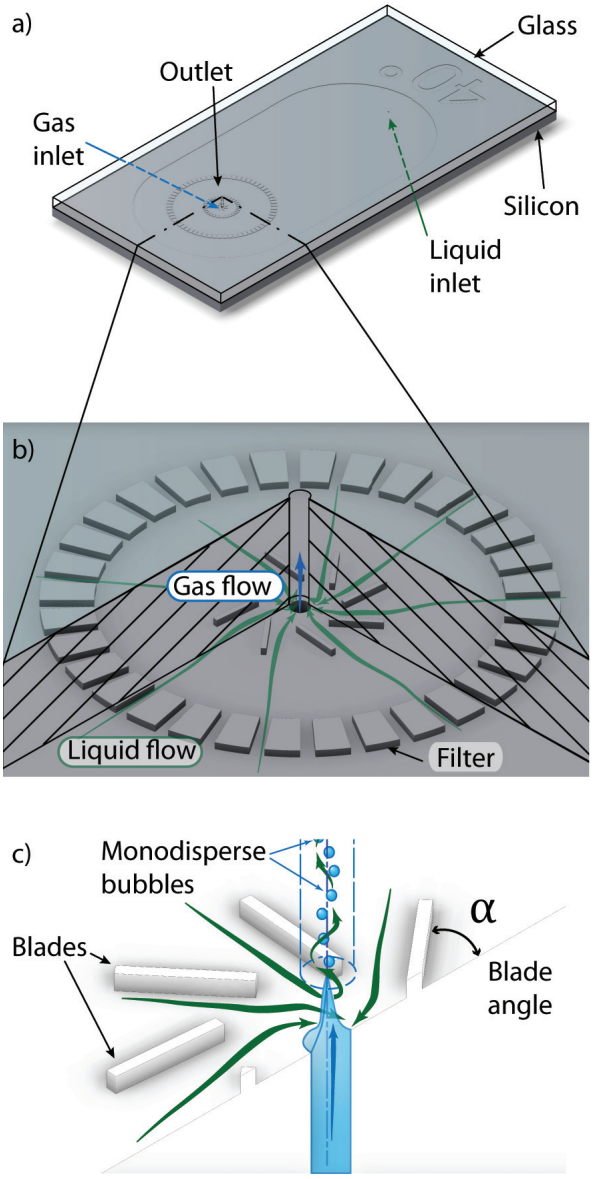

Figure 2.2: (a) Sketch of the swirl flow-focusing microfluidic device. (b) Closer view displaying the inner filter and the circular blade array. (c) Sketch of the imposed swirl leading to the formation of a stable gas meniscus that breaks into monodisperse microbubbles.

On the silicon wafer, a 500 nm thick silicon oxide layer was grown by wet oxidation. Subsequently, the pattern of the microfluidic chamber was transferred via standard photolithography and plasma etching into the silicon oxide layer (Adixen AMS100; Adixen France). The photoresist was removed and a new photolithography step was performed with the mask containing the pattern of the inlet holes. Using deep reactive ion etching (Bosch process, Adixen AMS100; Adixen France) the $80\,\mu$m inlet holes were etched into the silicon until the silicon oxide on the backside of the wafer was reached. The photoresist was removed and the remaining silicon oxide layer was used as a hard mask to deep reactive ion etch the $H = 30\,\mu$m deep microfluidic chamber. After cleaning, the silicon oxide was removed by etching in 50% hydrofluoric acid and the wafer was oxidised a second time with the newly formed $1\,\mu$m thick oxide layer striped afterwards. These last steps were performed in order to remove any residual silicon structures smaller than $1\,\mu$m, which might have remained at the location of the inlet holes due to the combination of the two deep reactive ion etching steps.
Prior to bonding, the glass wafer and the silicon wafer were cleaned in a Piranha solution for 15 minutes. The wafer pair was aligned in a mask aligner (EV620 maskaligner; EVG Austria) and the anodic bonding was performed in a vacuum at 400° C for 1 hour with 800 Volt applied (EV-501 Anodic Bonder; EVG Austria). As a final step, the bonded wafer stack was diced into chips (Disco DAD 321, Disco Japan) with adhesive foil protecting the in and outlets from contamination.

2.2.2 Experimental setup

The swirl flow-focusing microfluidic device was mounted on a xyz stage for precise translation. A high-speed camera (Shimadzu HPV2) with a resolution of 312×260 px^2 when operated at an acquisition rate of 1 Mfps, combined with a flash light source (WalimexPro VC600), was placed perpendicularly to the glass outlet channel.

The continuous phase was Milli-Q water. The surface tension between air and water σ was lowered from 72 to 40 mN/m by adding a 2% (w/v) of Tween 80 (Sigma Aldrich) to the water. The liquid flow rate Q_l is controlled by means of a high-precision syringe pump (Model 11 Plus, Harvard Apparatus). The precise control of the gas flow rate Q_g requires imposing a pressure gradient p_g through a pressure regulator (11-818-100, Norgren) and is measured using a digital manometer (Digitron 2030P). To avoid fluctuations in the gas flow rate the air was injected through a fused silica tube with 0.2 m in length and $75\,\mu$m of inner diameter. In order to prevent channel clogging by dust particles, an in-line filter (Parker, $0.01\,\mu$m) was added to the gas flow line. The swirl flow-focusing chip is connected to the gas and liquid flow lines using peek Nanoports (Assemblies, Nanoport, Upchurch Scientific).

The bubble diameter d_b and bubbling frequency f_b of at least 100 images, are measured via image processing (ImageJ). Knowing d_b and f_b, the volumetric gas flow

rate is determined as $Q_g = \pi d_b^3 f_b/6$. For low gas to liquid flow rate ratios, where bubbles tend to have a more elongated shape, the equivalent diameter was likewise calculated.

2.3 Results and discussion

Monodisperse bubbles (polydispersity index PDI $\sim 5\%$) ranging in size between $6\,\mu$m and $110\,\mu$m and at a high production rate ($f_b \sim 10^5$ Hz) were generated. Bubbles with diameters below $13\,\mu$m experience a higher PDI due to the high-speed camera resolution. We accomplished ~ 1000 experimental points varying the liquid flow rate from $Q_l = 0.5$ ml/min to $Q_l = 1.75$ ml/min and selecting gas pressures from $p_g = 200$ mbar to $p_g = 2300$ mbar, corresponding to flow rate ratios between $Q_g/Q_l = 0.01$ and $Q_g/Q_l = 1$.

The chosen liquid flow rate range covered both, the bubbling regime (lower values) and the jetting regime (higher values). In presence of high liquid flow rates, specially above $Q_l = 1.75$ ml/min, bubble jet formation becomes increasingly susceptible to perturbations, preventing the meniscus formation due to gas compressibility effects and hydrodynamic feedback. Gas pressure was selected to ensure bubbling and was gradually decreased until no bubbles were ejected.For the range of liquid flow rates investigated here, $Re = \rho_l v_b D/\mu_l \sim O(700)$, being ρ_l and μ_l the liquid density and viscosity, respectively, and v_b the velocity of the bubbles at the exit channel. This estimation indicates that the flow at the exit channel is laminar.

Figure 2.3 shows the effect of increasing the liquid flow rate Q_l for a 60° blade SFF microfluidic device and a constant value of the gas pressure p_g confirming the VoF numerical predictions of Herrada and Gañán-Calvo (2009). Increasing the water flow rate results in smaller bubbles and higher breakup frequencies but also narrows the Q_l range where monodisperse bubbles can be generated. The same trends were experimentally observed for all the SSF microchip blade angles. Bubbles of 6 μm in diameter at a production rate of 2.14×10^5 Hz can be obtained when the 60° blade SFF microdevice is used under the appropriated operating conditions.

Figure 2.4 displays the effect of increasing the SFF microchip blade angle for a constant value of the gas to liquid flow rate ratio Q_g/Q_l. Accordingly to the VoF numerical simulations presented by Herrada and Gañán-Calvo (2009), larger values of the SFF microchip blade angle results in smaller bubbles and higher breakup frequencies but also restricts the Q_l range where monodisperse bubbles can be generated.

In order to have a reference case for the comparison between different blade angles, a 0° SFF device was fabricated. If a conventional FF device is compared with a SFF, the breakup mechanism and the pressure drop might be completely different and the achieved reduction in bubble size could not be correctly accounted for. A reduction up to 57% in the microbubble diameter is accomplished when compared to a 0° SFF.

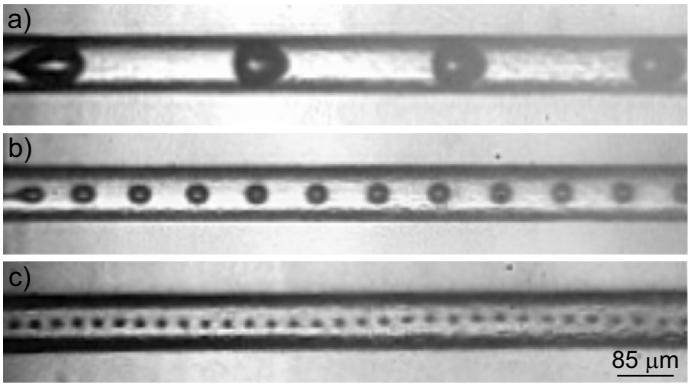

Figure 2.3: Series of images showing the effect of increasing the liquid flow rate for a 60° blade swirl flow-focusing microfluidic device and a constant value of the gas pressure: (a) $Q_l = 0.5$ ml/min, $p_g = 851$ mbar, $d_b = 77.03\,\mu$m, $f_b = 1.01 \times 10^4$ Hz; (b) $Q_l = 1$ ml/min, $p_g = 876$ mbar, $d_b = 36.57\,\mu$m, $f_b = 8.11 \times 10^4$ Hz; (c) $Q_l = 1.5$ ml/min, $p_g = 847$ mbar, $d_b = 13.17\,\mu$m, $f_b = 2.92 \times 10^5$ Hz.

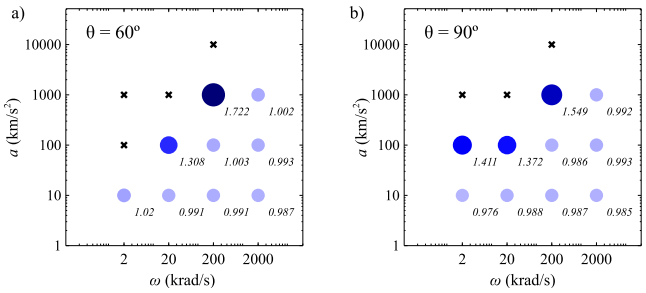

Figure 2.4: Series of images showing the effect of increasing the swirl flow-focusing microfluidic device blade angle for a constant gas to liquid flow rate ratio $Q_g/Q_l = 0.07$: (a) 0°, $Q_l = 1$ ml/min, $d_b = 45.15\,\mu$m, $f_b = 2.42 \times 10^4$ Hz; (b) 40°, $Q_l = 1.25$ ml/min, $d_b = 28.64\,\mu$m, $f_b = 1.19 \times 10^5$ Hz; (c) 60°, $Q_l = 1.5$ ml/min, $d_b = 23.72\,\mu$m, $f_b = 2.5 \times 10^5$ Hz.

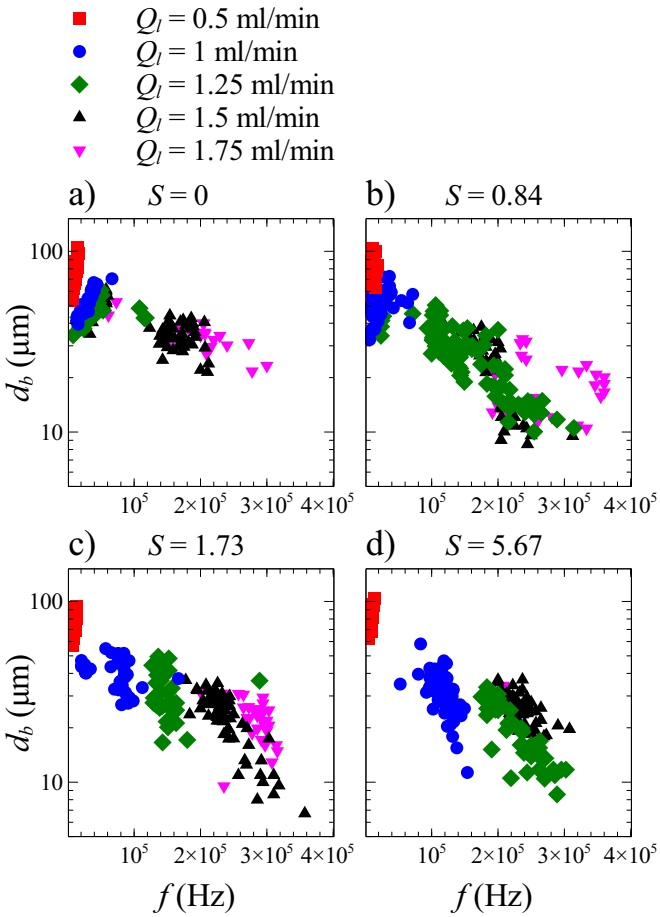

Figure 2.5: Bubble diameter versus microbubble production frequency for different blade angles. The indicated swirl factor S is the tangent of the blade angle in this work. The color codes for each liquid flow rate are also indicated.

Figure 2.5 shows the bubble diameter d_b (μm) versus microbubble production frequency f_b (Hz), for different blade angles. The effect of the swirl is clearly shown in this figure: the swirl factor is defined as $S = \tan(\alpha)$. This factor is expected to be approximately concurrent with that defined in Herrada and Gañán-Calvo (2009), since the blade angle α approximately defines the ratio of tangential to radial speeds. According to conservation of mass and angular momentum (excluding the many different boundary layer effects taking place), this ratio is expected to be approximately conserved when the liquid is eventually discharged through the outlet channel. In the absence of swirl (Figure 2.5(a)) the bubble size is modestly reduced by increasing the frequency of bubbling (i.e. reducing the gas flow rate). In contrast, a drastic decrease in the bubble size can be observed in the presence of swirl (Figure 2.5(b)) around a critical frequency range, indicating a transition associated to the stabilization of the gas meniscus and the presence of jetting. This is coincident with what was described in Herrada and Gañán-Calvo (2009). One can also observe that the increase of swirl (figures 2.5(c) & (d)), or the liquid flow rate over certain levels do not necessarily afford much better results in terms of a clear and reproducible decrease of bubble size, owing to the increase flow instabilities and incipient turbulence.

To further represent our results in the framework of prior physical understanding, Figure 2.6 depicts the microbubble diameter normalized with the exit channel diameter d_b/D as a function of the gas to liquid flow rate ratio Q_g/Q_l for different SFF microchip blade angles (0°, 40°, 60° and 80°) and three representative liquid flow rates (Q_l =0.5, 1 and 1.5 ml/min). The figure shows two perfectly differentiable trends related to the two existing regimes. The experimental points corresponding to a bubbling regime, where no stable meniscus is created, are in the upper blue region, above the black solid line. By contrast, the experimental points where the combination of the swirl and flow-focusing effects enables the formation of a stable meniscus are in the lower green region, following the black solid line. In the latter situation, bubbles considerably smaller than the characteristic geometric length are ejected.

The black solid line in Figure 2.6 represents the scaling law presented by Gañán-Calvo (2004) using conventional axisymmetric flow-focusing devices

$$d_b/D = \eta \, (Q_g/Q_l)^{0.4}, \tag{2.1}$$

where $\eta = 1.1$ is a universal constant. In this work, we have found a slight deviation ($\eta = 0.9$) in the coefficient proposed by Gañán-Calvo (2004) due to a *vena contracta* effect. The high aspect ratio between the chip chamber height H and the exit channel diameter D, combined with the sharp edge of the entrance of the exit channel leads to a smaller effective exit diameter. The inclusion of the two colored regions constitutes a visual help to easily distinguish between the bubbling and the jetting regimes. The intent is not to give an exact separation (since transitions are never neat) but to be an eye guide for the reader. The straight boundary is chosen accordingly to the power-law

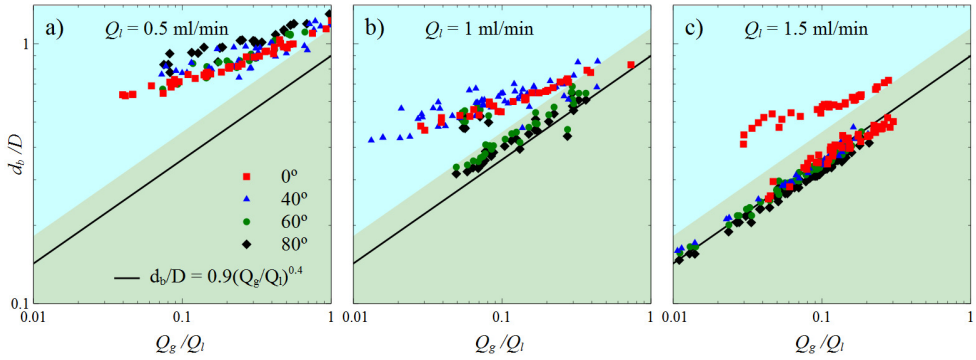

Figure 2.6: Dimensionless bubble diameter versus gas to liquid flow rate ratio for different microchip blade angles and increasing values of the liquid flow rate: a) $Q_l = 0.5$ ml/min; b) $Q_l = 1$ ml/min; c) $Q_l = 1.5$ ml/min. The black solid line is the power-law fit proposed by Gañán-Calvo (2004). The upper blue region corresponds to a bubbling regime whereas the lower green region relates to a jetting regime. The colored regions are not an exact boundary but an eye guide for the reader to easily distinguish between the bubbling and the jetting regimes.

fit proposed by Gañán-Calvo (2004) which is followed by our experiments. The same boundary is used for the three plots in Figure 2.6.

The figure also manifests that both regimes, bubbling and jetting, can be obtained for a particular gas to liquid flow rate ratio and a given SFF microchip blade angle. Not only is gas to liquid flow rate ratio (Q_g/Q_l) relevant to reach a jetting regime, but also their absolute flow rates (Q_g and Q_l). For instance, in Figure 2.6 (c) for a gas to liquid flow rate ratio $Q_g/Q_l = 0.1$ we have two completely different experimental points: (i) a microbubble produced in the bubbling regime with a dimensionless bubble diameter $d_b/D = 0.57$, a gas flow rate $Q_g = 0.15$ ml/min, a liquid flow rate $Q_l = 1.5$ ml/min and a production rate $f_b = 4.16 \times 10^4$ Hz and (ii) a microbubble produced in the jetting regime with a dimensionless bubble diameter $d_b/D = 0.37$, a gas flow rate $Q_g = 0.14$ ml/min, a liquid flow rate $Q_l = 1.5$ ml/min and a production rate $f_b = 1.42 \times 10^5$ Hz. The transition between both regimes is a delicate boundary that can be crossed with a change in gas pressure of just a few milibars. This sensitivity to small changes is especially present for a blade angle equal to 0°. As soon as the blade angle increases, the possibility of two different regimes for similar operating conditions disappears, which strongly reinforces the convenience of the swirl flow-focusing configuration.

The transition from bubbling to jetting regime can be accomplished (for a fixed geometry and fluids) by increasing the liquid flow rate, as it was previously seen in Figure 2.3. Our experimental study demonstrates that this transition can also be conducted imposing a swirl on the liquid. Both effects are comprised in Figure 2.6:

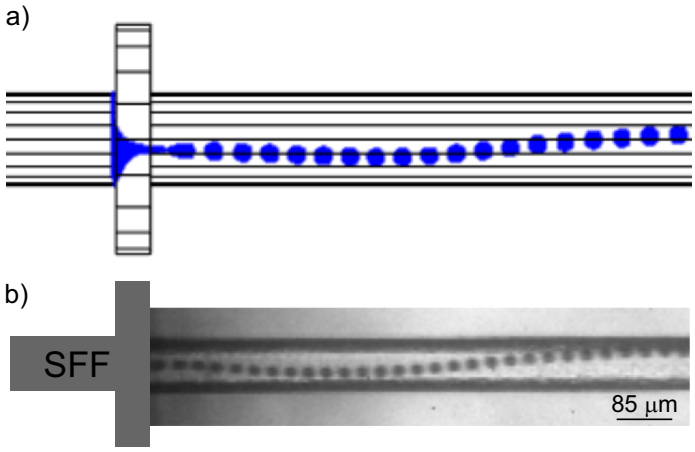

Figure 2.7: (a) Numerical simulation illustrating an undulating bubble train. (b) Image showing the experimental undulating bubble train for a 40° blade angle SFF microdevice, $Q_l = 1.75$ ml/min, $p_g = 1341$ mbar, $d_b = 18.45\,\mu$m, $f_b = 3.6 \times 10^5$ Hz.

the increase of liquid flow rate and microchip blade angle. Furthermore, the stronger the swirl is, i.e. higher the blades angle, the lower liquid flow rates are needed to work on jetting conditions. Thus, the shift to jetting is reached more easily thanks to the imposed swirl. The transition occurs around $Q_l = 1.5$ ml/min using $0\,^\circ$ blade angle chips, but decreases to 1.25 ml/min for $40\,^\circ$ blade angle microchips and to 1 ml/min for $60\,^\circ$ and $80\,^\circ$ microdevices. We observed a plateau on the swirl general performance above $60\,^\circ$ blade angle, related to the previously observed drastic decrease of the effect of swirl over an optimal strength (see Herrada and Gañán-Calvo (2009)). Part of that decrease could be attributed to the enhancement of perturbations.

Figure 2.7 shows the bubble train undulation predicted by the VoF numerical simulations and its experimental observation. The simulation was previously obtained by Herrada and Gañán-Calvo (2009) for pure water (without surfactant) and imposing numerically a swirl on a conventional axisymmetric Flow-Focusing device. This undulation is due to experimental perturbations, such as dust particles, that may disrupt the axial symmetry of the jet. It also confirms that there is no bubble size change despite the trajectory deviation, which was forced in the simulations and naturally occurred in some experimental cases. The helicoidal trace followed by the bubbles is the result of the imposed liquid swirl, migrating the bubbles towards the regions of lower pressure at the axis of the liquid vortex.

Lastly, experiments with ultra-pure MiliQ water (without surfactant) were also conducted. The results showed an overall similar behavior, although the increase of surface tension favored the presence of hydrodynamic feedback. Consequently, the accessible flow rate ratios range was drastically reduced.

2.4 Conclusions

A novel swirl flow-focusing microfluidic device for the production of monodisperse microbubbles at a high production rate is presented. The swirl effect is achieved thanks to the rotation induced by a circular array of microblades turned a certain angle. The addition of a swirl component into the focusing liquid stabilizes the gas meniscus from which a steady gas ligament issues breaking into monodisperse microbubbles. Furthermore, the swirl is shown to expand the bounds of the jetting mode inhibiting the dripping mode. As consequence of the extension of the jetting regime, a reduction up to 57% in the microbubble diameter is accomplished when compared to conventional axisymmetric flow-focusing microdevices.

Inspired by the numerical results of Herrada and Gañán-Calvo (2009) and Herrada et al (2011), we perform 3D CFD simulations (FLUENT) to determine the most promising geometric dimensions for the swirl flow-focusing microdevices. Based on the simulations, silicon microchips with blade angles 0°, 40°, 60° and 80° were fabricated. Working under the appropriate experimental conditions, monodisperse bubbles (PDI $\sim 5\%$) ranging in size between $6\,\mu$m and $110\,\mu$m and at high production rate ($f_b \sim 10^5$ Hz) can be generated. An exhaustive experimental study (~ 1000 experimental points) is performed validating previous VoF numerical simulations and complying with the flow-focusing scaling law proposed by Gañán-Calvo (2004). The 60° swirl flow-focusing microfluidic device shows the best performance, among our tested chips, with a trade off between swirl effect and robustness against perturbations.

References

Anna SL, Bontoux N, Stone HA (2003) Formation of dispersions using flow focusing in microchannels. Applied Physics Letters 82(3):364–366

Castro-Hernández E, van Hoeve W, Lohse D, Gordillo JM (2011) Microbubble generation in a co-flow device operated in a new regime. Lab on a Chip 11(12):2023–2029

Dollet B, Van Hoeve W, Raven JP, Marmottant P, Versluis M (2008) Role of the channel geometry on the bubble pinch-off in flow-focusing devices. Physical Review Letters 100(3):034504

Ferrara K, Pollard R, Borden M (2007) Ultrasound microbubble contrast agents: fundamentals and application to gene and drug delivery. Annu Rev Biomed Eng 9:415–447

Gañán-Calvo AM (2004) Perfectly monodisperse microbubbling by capillary flow

focusing: An alternate physical description and universal scaling. Physical Review E 69(2):027301

Gañán-Calvo AM, Gordillo JM (2001) Perfectly monodisperse microbubbling by capillary flow focusing. Physical Review Letters 87(27):274501

Gañán-Calvo AM, Herrada MA, Garstecki P (2006) Bubbling in unbounded coflowing liquids. Physical Review Letters 96(12):124504

Garstecki P, Gitlin I, Diluzio W, Kumacheva E, Stone HA, Whitesides GM (2004) Formation of monodisperse bubbles in a microfluidic flow-focusing device. Applied Physics Letters 85:2649–2651

Garstecki P, Gañán-Calvo A, Whitesides G (2005) Formation of bubbles and droplets in microfluidic systems. Technical Sciences 53(4)

Garstecki P, Fuerstman MJ, Stone HA, Whitesides GM (2006) Formation of droplets and bubbles in a microfluidic t-junctionñscaling and mechanism of break-up. Lab on a Chip 6(3):437–446

Herrada MA, Gañán-Calvo AM (2009) Swirl flow focusing: A novel procedure for the massive production of monodisperse microbubbles. Physics of Fluids 21(4):042003

Herrada MA, Gañán-Calvo AM, López-Herrera JM (2011) Generation of small monodisperse bubbles in axisymmetric t-junction: the role of swirl. Physics of Fluids 23(7):072004

Kennedy J, Wu F, Ter Haar G, Gleeson F, Phillips R, Middleton M, Cranston D (2004) High-intensity focused ultrasound for the treatment of liver tumours. Ultrasonics 42(1-9):931–935

Marmottant P, Van Der Meer S, Emmer M, Versluis M, De Jong N, Hilgenfeldt S, Lohse D (2005) A model for large amplitude oscillations of coated bubbles accounting for buckling and rupture. Journal of the Acoustical Society of America 118(6):3499–3505

Takahashi M (2005) Potential of microbubbles in aqueous solutions: Electrical properties of the gas - water interface. Journal of Physical Chemistry B 109(46):21858–21864

Wei K, Jayaweera A, Firoozan S, Linka A, Skyba D, Kaul S (1998) Quantification of myocardial blood flow with ultrasound-induced destruction of microbubbles administered as a constant venous infusion. Circulation 97(5):473–483

Whitesides G (2006) The origins and the future of microfluidics. Nature 442(7101):368–373

3

A theoretical study on acoustic control of microbubbles in planar flow focusing*

Microbubble generation in microfluidic systems can be controlled via either active or passive means. An example of active control is the mechanical excitation through the induction of an acoustic streaming. Acoustic excitation has attracted significant interest for tuning bubble size and has been studied experimentally. However, a theoretical framework for the physics and parametric description of that tuning is not ready yet. Computational analysis is currently an invaluable tool but few studies have been reported so far. In this work, the generation of microbubbles in planar flow focusing is numerically analyzed for an ample range of acoustic accelerations and frequencies and for several contact angles. The effects on the formation and size of the generated microbubble is investigated in the assumption of negligible gas compressibility. The contact angle is found to have an influence of circa 20% on the bubble volume, confirming its relevance. When applying acoustic excitation, the bubble volume increases with the excitation amplitude until the system collapses by unrealistic incompressibility demands. A theoretical dimensional analysis is performed, and a key parameter is identified that exhibits a critical value for which the volume reaches a maximum before the system collapses. Last, this study highlights current critical capabilities and limitations of 3D CFD modeling techniques for microfluidic multiphase flow devices.

*Submitted to Microfluidics and Nanofluidics as: Irene Arcos-Turmo, Miguel A. Herrada, Say Hwa Tan, Alfonso M. Gañán-Calvo: "A theoretical study on acoustic control of microbubbles in planar flow focusing".

3.1 Introduction

Microbubbles are critical in an immense variety of natural and artificial phenomena and their applications. Their intentional generation can be controlled by either active or passive means. Exerting passive control of bubble size is limited to geometrical design of devices (Herrada et al, 2015) or varying hydrodynamic forces, commonly implemented by either controlling the pressures or flow rates of both gas and liquid carrier for a given set of liquid properties (Gordillo et al, 2001; Garstecki et al, 2004; Martinez, 2009; Castro-Hernández et al, 2011). Active ways introduce a third variable to control the system, such as magnetic, mechanical or electric forces, deeply studied in droplet generation (Chong et al, 2016). Previous work done by Chong et al (2015) revealed possible ways of controlling bubble size and distribution by means of an acoustic input. They found a bubble volume increase for certain values of the acoustic excitation. The experimental results showed a dramatic increase of the bubble size at various excitation amplitudes corresponding to the resonance frequencies of the piezoelectric transducer. The reported new active mechanical control could be of considerable interest for tuning bubble size, given the fast response of the system, in the order of 100 ms, and constitutes a cornerstone for the present research. Nevertheless, just a single excitation case was then analyzed.

A better understanding of the system response to excitation is of considerable interest, specially if bubble size can be tuned by changing the acoustic excitation parameters. Here, a first fundamental issue associated to the relative scales of normal mode frequencies and excitation frequencies appear. In turn, normal modes gauge the relative weight of gas compressibility, surface tension σ and flow streaming effects. The first mode, corresponding to the lower frequency mode, is fundamentally associated to the commensurate scales of gas compressibility and liquid inertia; its frequency ω_o is then proportional to $\sqrt{P_{\mathrm{eq}}/(\rho R_{\mathrm{o}}^2)}$ (Plesset and Prosperetti, 1977), where P_{eq} is the internal gas pressure at equilibrium, ρ the liquid density, and R_{o} the equivalent bubble radius. Higher modes fundamentally correspond to conditions –with an increasing number of surface nodes– for which surface waves and surrounding streaming around the attached issuing bubble resonate (Gañán-Calvo, 1991), which yields natural frequencies proportional to $\sigma/(\rho R_{\mathrm{o}}^3)$ with a prefactor that is proportional, in turn, to the number of nodes.

Cavitation and enhanced ultrasound effects require excitation frequencies close to the one of the first normal mode. These effects are forced in many applications following different approaches; for example, introducing acoustic excitation with a relatively ample spectrum of frequencies in polydisperse bubble solutions or using bubble shoals with more or less uniform size and a single excitation frequency. On the other hand, gas bubbles or vapor nucleation points of a certain scale (be those microbubbles or surface irregularities) should obviously be present in cavitation. Thus, mass production of microbubbles is in most cases a nearly universal main step

in technologies using acoustic enhancement effects in multiple applications. Here, microfluidics is technologically positioned at the top of potential solutions for mass generation of microbubbles.

Producing bubbles of a controlled size by gas injection from a channel involves the cyclic growth of bubbles attached to the channel outlet and their subsequent cyclic detachment. During that growth and applying a fixed excitation frequency, the bubble may reach a point of resonance. That detachment would result in stronger oscillations, which suggests a way to control bubble size by the acoustic excitation of the system at a certain frequency comparable to the first mode of the bubbles with desired size. However, this simple idea finds a plethora of issues in its materialization. First, the complexity of the channel outlet geometry at the point of intersection with the ones of the carrier liquid, together with crucial effects like static-dynamic contact angles, contact lines or anchorage conditions, makes the determination of resonance frequencies extremely difficult and case-dependent. Second, introducing the acoustic excitation is not a trivial issue since its frequency and amplitude are not the only available degrees of freedom: the corresponding acceleration can be induced in any three dimensional direction; in most cases, that direction is not even known a priori when a piezoelectric actuator is attached to the system, since the latter affects the dynamics of the former and viceversa.

Therefore, numerical simulations may be a feasible and probably the only viable option to investigate the effect of the particular features of each system in the microfluidic generation of microbubbles. Microfluidic simulations are increasingly popular due to its cost and accessibility, allowing a better understanding and precise control of the modeled system. Multiflow simulations have been reported for axisymmetric flow focusing (Herrada et al, 2011), cross-junctions (Salari and Dalton, 2015; Chinnov et al, 2016), T-junctions (Santos and Kawaji, 2012; Vega et al, 2014) and other devices. Different Multiflow models are employed, such as VOF and the Level Set Method (Chen et al, 2007; Wörner, 2012). However, very few full three-dimensional simulations have been reported till date (Cubaud et al, 2005; Dai et al, 2009; Santos and Kawaji, 2010b; Herrada et al, 2013), most of them with axisymmetric conditions (Herrada et al, 2011; Vega et al, 2014).

An overall consideration of the main issues arising in the three-dimensional numerical simulation of these systems points to contact angle and attachment conditions as the principal sources of variability, sensitivity and discrepancies with experiments. Here, one of the best current reviews on wetting-dewetting, static and dynamic contact angles, and contact lines is described by Bonn et al (2009). The complexity of the subject has hampered its appropriate implementation in current commercial CFD software, though. In spite of this, the use of a macroscopic contact angle in the dynamics of multiphase microfluidics is probably a commonplace in the analysis of a vast majority of phenomena ranging from short to long timescales. Thus, to reasonably circumvent

the complexity associated to the detailed analysis of a multiplicity of effects (down to the molecular scale) is to assume a certain value of the contact angle. This value should reflect the majority of associated effects observed for a given system. This idea implies the investigation on those effects varying the contact angle as a free parameter, observing for which value range a simulated system furnishes the best resemblance of its real counterpart. If the real system is then subject to changes in surface tension or wettability conditions, one can follow the same procedure to reflect those changes in the contact angle. This procedure may allow the construction of valuable models for CFD simulations of multiphase microfluidics systems.

In this work, the dependence of the contact angle and the applied acoustic excitation on the formation of microbubbles in a microfluidic planar flow focusing, more concretely a cross-junction, is studied using numerical simulations. Full 3D numerical simulations are performed to model the microbubble generation process. To this end, in the absence of any available alternative in existing software, we assume that a macroscopic overall value of the contact angle should reasonably match observation and simulation for a wide range of time scales. This study also reveals potential explanations of the physic involved, highlighting a clear range for contact angle values where simulations and observations agree well.

3.2 Problem definition

A planar cross-junction microdevice with a rectangular channel section of $100\,\mu\text{m}\times 43\,\mu\text{m}$, similar in geometry and dimensions to those employed by Chong et al (2015) in a previous experimental work was selected. Inlet lengths were chosen so as to achieve full laminar developed flow, see Figure 3.1. The cross-section was simplified to one quarter due to symmetry. As for the phases, nitrogen gas (density $\rho_\text{g} = 1.138\,\text{kg/m}^3$, dynamic viscosity $\mu_\text{g} = 1.663\times 10^{-5}\,\text{kg/ms}$) and mineral oil (density $\rho_\text{l} = 840\,\text{kg/m}^3$, dynamic viscosity $\mu_\text{l} = 0.03\,\text{kg/ms}$) were chosen as the disperse phase and continuous phase, respectively. Nitrogen is injected along the central channel in order to form the microbubbles, whereas the mineral oil is perpendicularly introduced. Mineral oil flow rate was fixed to $Q_\text{l} = 960\,\mu\text{l/h}$ and nitrogen gas flow rate to $Q_\text{g} = 302\,\mu\text{l/h}$.

3.2.1 Contact angle

Surface tension, and thereby the contact angle, plays a fundamental role when dealing with microfluidic devices. In microfluidics, where the surface to volume ratio increases, inertia is overcome by viscous and interfacial forces. As previously mentioned, despite the importance of the surface tension forces, the dynamic contact-angle treatment in numerical commercial software is still underdeveloped. As an example, Fluent contact

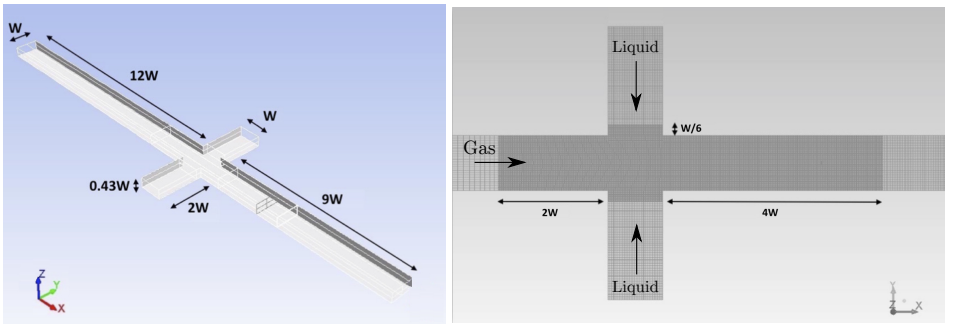

Figure 3.1: (a) Sketch of the numerical three-dimensional cross-junction geometry. $W = 100\,\mu$m. (b) Closer view displaying the one-refinement mesh region dimensions.

angle treatment is currently restricted to the imposition of a constant body force term at the Momentum equations. This term reflects the macroscopic effect of molecular interactions of the different fluid species with the wall, leading to an effective contact angle value when equilibrium is imposed at the cells where the three-phase contact line is located. Specifically, it is formulated as:

$$\begin{aligned} &\frac{\partial \rho}{\partial t} + \nabla\cdot(\rho\vec{v}) = 0 \\ &\frac{\partial(\rho\vec{v})}{\partial t} + \nabla\cdot(\rho\vec{v}\vec{v}) = -\nabla p + \nabla\cdot[\mu(\nabla\vec{v} + \nabla\vec{v}^T)] + \vec{F} \\ &\frac{\partial \Omega_i}{\partial t} + \vec{v}\cdot\nabla\Omega_i = 0, \end{aligned} \tag{3.1}$$

where Ω_i defines the local phase fraction between phases: given the $i-$phase, $\Omega_i = 1$ in the $i-$phase domain and $\Omega_i = 0$ otherwise. Phase continuity demands $\sum_i \Omega_i = 1$ everywhere. The term $\vec{F}$ is the aforementioned body force term. This formulation excludes the dynamic contact angle as well as the micro-liquid channel that could actually be formed between the bubbles and the wall, which was deeply studied by Ajaev and Homsy (2006) and Santos and Kawaji (2012). Such film provides lubrication of the channel wall and enhances velocity slip. Thus, interface pinning is more probable to occur in our simulation due to the present software. Moreover, the contact angle between mineral oil, nitrogen gas and PDMS, which has to be fixed for the simulations, is unknown a priori. Therefore, the dependence of the contact angle on the bubble size is of highly valuable knowledge and constitute a fitting variable or degree of freedom to fit the experiments. Thus, the effect of static contact angles between 25° and 120° on the generated bubble size is analyzed, where the static contact angle is defined as shown in Figure 3.2.

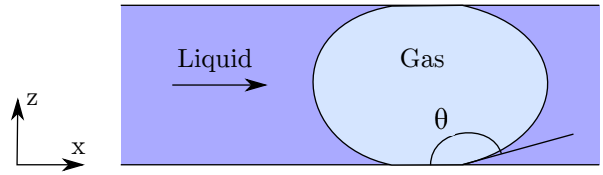

Figure 3.2: Contact angle definition. Side view of the cross-junction channel.

3.2.2 Acoustic Excitation

The acoustic excitation was modeled as a body force in the longitudinal direction x, with a sinusoidal form of frequency ω and acceleration amplitude, called amplitude, a, from this point forward. The body force was imposed as a source term using a User Define Function (UDF). The entire domain is subject to exactly the same imposed acceleration since the smallest wavelength in the solid corresponding to the largest studied excitation frequency is about one order of magnitude larger than the computational domain size. To rate the initial values of the both variables, Reynolds, Weber, and Capillary numbers at the cross junction were estimated. Defined as

$$Re = \frac{\rho_l v_l W}{\mu_l}, We = \frac{\rho_l v_l^2 W}{\sigma}, Ca = \frac{We}{Re} = \frac{\mu_l v_l}{\sigma},$$

where ρ_l and μ_l are the density and viscosity of the continuous phase, σ is the surface tension, v_l is the liquid velocity computed at the entrance and W the characteristic length of the channel, the predominance of interfacial and viscous over inertia forces was confirmed and laminar conditions were proved, with Re $\backsim 10^{-2}$, We $\backsim 10^{-3}$, and Ca $\backsim 10^{-2}$. The acoustic excitation amplitude a was selected to overcome both, viscous and interfacial forces. First, an estimation to overcome the viscous forces was obtained by balancing the Navier-Stokes viscous and mass acceleration terms,

$$a \backsim \frac{\mu_l v_l}{\rho_l W^2}, \tag{3.2}$$

which leads to an excitation amplitude of $\sim 2.000\,\mathrm{m/s^2}$. Likewise, the critical Bond number, $Bo_{cr} = (\rho_l \Delta a W^2)/\sigma \backsim 1$, which correlates body and interfacial forces, lead to an amplitude term of $\sim 6.000\,\mathrm{m/s^2}$, in order to overcome the surface tension forces.

As a result, acoustic excitations for amplitudes between $10.000\,\mathrm{m/s^2}$ and $10.000.000\,\mathrm{m/s^2}$ and frequencies between 2 krad/s and 2.000 krad/s were studied. The parametric exploration was composed of 26 cases (13 for each contact angle).

3.3 Numerical methods

Three-dimensional numerical simulations were accomplished using FLUENT CFD Software provided by ANSYS 15.0.0 and a 68-processadors cluster. An unsteady pressure-based solver with double precision was used. VOF multiphase model (Volume of fluid) based on an explicit time-marching scheme and an implicit body force formulation was selected. This decreases diffusion while lightened the computational time by means of the Courant number. The Courant number for each simulation step is defined as $C = u\Delta t/\Delta x$, being Δt the time step, Δx the space interval and u the velocity computed at each element. To ensure convergence, time steps ranging from 10^{-7} s to 10^{-12} s were automatically adapted to ensure a global Courant number lower than 0.5. SIMPLE scheme was chosen for the Pressure-velocity coupling and equations were spatially discretized with Least Squares Cell Based for the Gradients, PRESTO! (Pressure staggering options) for the pressure and Second Order Upwind for the Momentum. The transient formulation was solved using the First order implicit scheme.

Mass flow boundary conditions were employed for both inlets and Pressure outlet for the channel exit. Modeling the gas inlet with Mass flow instead of Pressure inlet boundary condition avoids pressure oscillations from moving upstream, which would required a longer gas inlet channel to reduce them and thus, a significant increase in the computational cost. Likewise, the exit channel, the time-bottleneck of the simulations, was modeled as Pressure outlet to reduce computational instabilities derived from the acoustic excitation.

The applied continuum surface force (CSF) model proposed by Brackbill et al (1992) takes into account the surface tension effects by introducing an extra body force term at the momentum equation. The static contact angle and surface tension ($\sigma = 0.033$ N/m) have to be prescribed in advance (Wall adhesion model). Instead of forcing a constant contact angle at the wall, it adjusts the interface normal of the cells near the wall using the static contact angle, adjusting the curvature near the wall and calculating the body force term previously mentioned (Santos and Kawaji, 2010a).

3.3.1 Mesh Quality vs. Computational Time

Interface tracking in multiphase flow problems requires full 3D-models to achieve reliable and representative results (Santos and Kawaji, 2010b). Nevertheless, this increases computational cost both drastically and exponentially. In the present study, with high viscosity and an excitation of considerable frequency and acceleration, mesh optimization becomes crucial and both, elements type and size, have to be carefully chosen. The larger the element, the higher the numerical diffusion and tracking errors. Quadrilateral elements are selected for a better solution convergence taking advantage of the Workbench meshing software. Preliminary runs with a coarse or basic mesh

were performed to achieve a better convergence while reducing computational cost. Afterwards, the cross-junction region was adapted up to two times, reducing the original element size by four. Figure 3.1 displays the cross-junction and refined region dimensions. Element size ranged from $1.48\,\mu$m for the basic mesh to $0.36\,\mu$m for the two-refinements mesh. The implementation of an even finer mesh was rejected due to its disproportional high computational cost. As a rule of thumb, simulation time cost using the basic mesh is of the order of days, whereas one-refinement simulations require more than a week and more than a month when using two-refinements mesh.

3.3.2 Compressibility assessment

Gas density variations with respect to its density, $\delta\rho_g/\rho_g$, of 5% is generally accepted as the incompressible limit. Numerical runs modeling the disperse phase as a compressible fluid –Energy model– were performed before analyzing the acoustic excitation influence. Considering a fixed gas flow rate, non-volumetric bubble oscillations should only be observed for an incompressible case, while a total bubble volume fluctuation –corresponding to a volumetric mode– would be measured if compressible phenomenon occurred. Cases centered in the studied excitation region ($\omega = 200\,$krad/s, $a = 100.000\,$m/s^2) were selected and their total bubble volume monitored, confirming a $\delta V_g/V_g < 2.5\%$. The acoustic excitation problem was therefore modeled as incompressible, substantially reducing its computational cost.

3.4 Results

The bubble volume V was directly computed using the above simulation method. The outlet gas flow rate was monitorized and compared with the inlet gas flow as a control mechanism to account for numerical errors, reflecting flow rate deviations lower than 2.5%. The bubble diameter d_b was computed as $d_b = (6V/\pi)^{1/3}$. For cases where bubbles tend to have a more elongated shape, the equivalent diameter was likewise calculated. Monodisperse bubbles (PDI $\leq 1.15\%$), ranging in size between $84\,\mu$m and $93\,\mu$m, at a production rate of $\omega_g \sim 10^3$ rad/s were generated.

3.4.1 Contact angle

Figure 3.3 displays the microbubble diameter normalized with the channel width W as a function of the imposed contact angle θ –for different mesh refinements–, accounting for both, mesh sensitivity analysis and contact angle influence. The system experiences a decreasingly bubble volume increase when the element size is reduced. The biggest bubble volume difference between the cases with basic mesh and those with one refinement is of 11%. However, this difference drops to 1.7% between cases with one and two refinements. Due to the increasing computational cost and being

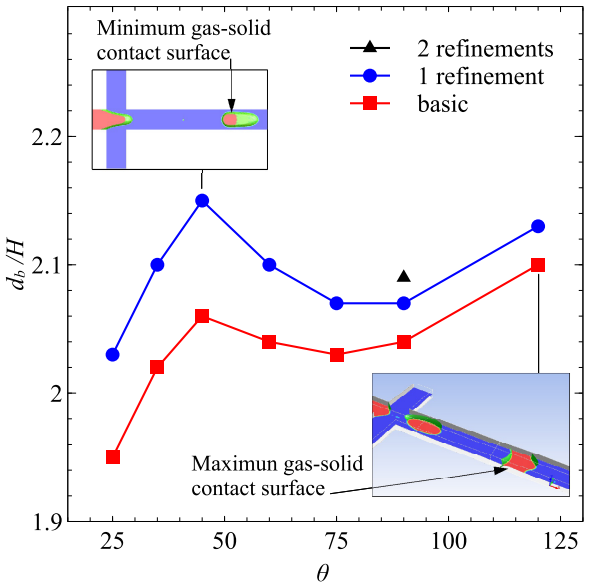

Figure 3.3: Microbubble diameter normalized with the channel width W as a function of the imposed contact angle θ for different mesh refinements. Basic mesh element size is 1.48 μm, one-refinement mesh 0.74 μm and two-refinements mesh 0.36 μm.

the bubble size results with two and one refinements quite similar, we determined that reliable results for studying the excitation behavior could be obtained based on one refinement. In fact, the mesh is seen to have little effect on the fluid dynamic behavior of the system, ratifying our assumptions. Moreover, this choice reduces numerical instabilities appearing at the mesh transition between the refined region and the following non-refined exit channel, specially decisive when the bubble leaves the refined domain. Two critical points are detected when incrementing the contact angle: a first one, at 45°, corresponding to the point in which the generated bubbles start wetting the upper and lower walls of the exit channel cross section; and a second point, at 120°, in which the bubbles wet the four exit channel walls. By varying the contact angle, the microbubble volume can differ as much as 21.4% –for the basic mesh– and 17% –for the refined mesh–. The subsequent simulations applying acoustic excitation were performed for 60° and 90° with one refinement, which best fitted the experimental observations obtained by Chong et al (2015).

3.4.2 Acoustic excitation

The parametric sweep was composed of 25 cases. Figure 3.4 depicts the microbubble volume with excitation, V_{ex}, normalized by its volume without acoustic excitation, V,

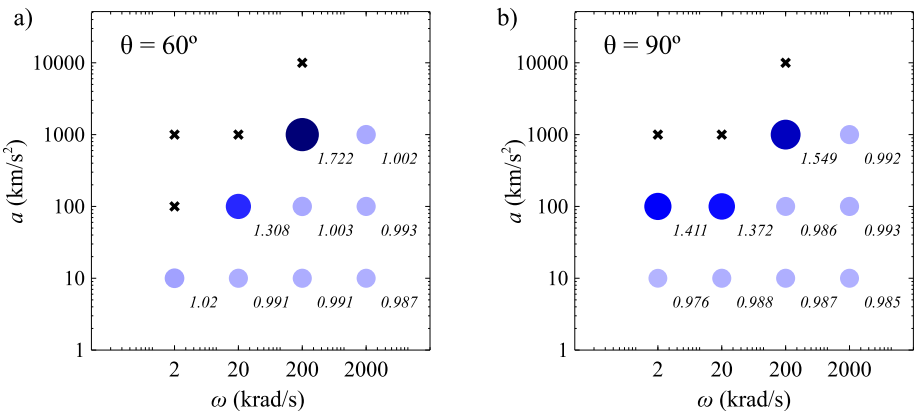

Figure 3.4: Dimensionless bubble volume V_{ex}/V as a function of the imposed amplitude a and frequency ω with contact angle of a) 60° and b) 90°. Black crosses represent cases that collapsed. Blue color darkness is proportional to V_{ex}/V.

as a function of the imposed amplitude a and frequency ω and for the selected contact angles: 60° and 90°. Circles size and color are proportional to the normalized bubble volume, V_{ex}/V. Microbubble size increases with excitation amplitude until a limit where the cases collapsed, represented by black crosses. The largest bubble volume change due to acoustic excitation was of 72%. The PDI remained below 1.3% except for the limit cases –those for which an amplitude increment would lead to collapse–. Those limit cases could experience a PDI increment of up to 17%, showing a less monodisperse behavior. The excitation frequency is correlated with the maximum amplitude that the system can absorb but has otherwise little effect on the bubble volume: the higher the frequency, the higher the amplitude that the system can absorb. Figure 3.5 shows an example of the bubble generation where the bubble oscillation can be observed (60° contact angle, $\omega = 20\,\text{krad/s}$ and $a = 100\,\text{km/s}^2$) in comparison with the same case without acoustic excitation.

Besides, the closer the excitation frequency is to the generation frequency ($\omega_g \sim 1275\,\text{rad/s}$ on average), the more crucial the moment in which the excitation is added is, playing a vital role for the global stability of the system. Cases with an excitation frequency close to the generation frequency showed a sensible and chaotic behavior and were therefore avoided. Although not too close, an example of the latter behavior is the limit case of $\omega = 2\,\text{krad/s}$, $a = 100\,\text{km/s}^2$, where the generation process collapsed with 60°, whereas monodisperse bubbles were generated with 90°. In fact, a very stable production was found for the latter case because the moment in which the excitation was added allowed the backwards oscillation to match the pinch off.

The observed collapse can occur due to physical effects derived from the excitation, but mainly due to numerical reasons, such as the break down of the generated bubbles

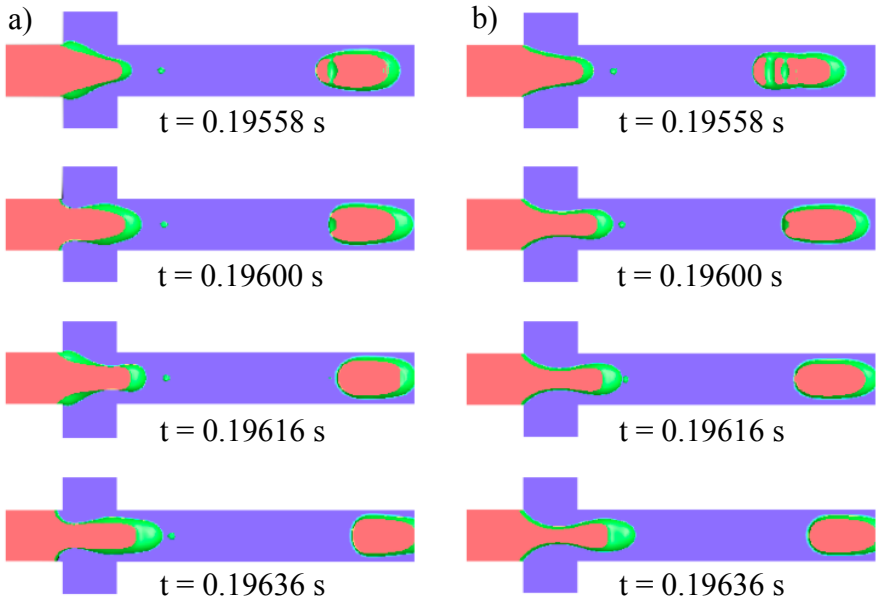

Figure 3.5: Series of images showing simulated bubble oscillation for 60° contact angle a) with an imposed acoustic excitation (ω=20 krad/s, a=100 km/s^2) and b) without acoustic excitation. In blue the carrier liquid, green the gas-liquid free surface and red the solid surface in contact with the gas.

into many tiny bubbles or because of a few mesh elements with incongruous velocities which develop in bubble break up. However, both cases are related. In experiments, gas compressibility plays a smoothing effect on the system. Nevertheless, the numerically imposed incompressibility, although overall correct, does not compensate pressure peaks that appear on certain short-term instants. As a result, the numerical collapse reveals in our study the limit from which incompressibility conditions can no longer be imposed.

3.4.3 Dimensional analysis

Our system is characterized by the liquid and gas properties (ρ_l, ρ_g, μ_l, μ_g and σ), the channel cross geometry (W and h, where $h = 0.43W$ in this work), the operating parameters (Q_g, Q_l), the contact angle θ, and the excitation parameters (ω, a). Gas density and viscosity play an irrelevant role on the bubble size compared to those of the liquid. Operating parameters Q_l and Q_g are kept constant in this study.

Initially, we evaluate the strength or nonlinear character of the induced capillary

waves. The two fundamental scales associated to the capillary waves are their characteristic wavelength λ and their capillary waves amplitude l_a. The radius of curvature associated to the capillary waves is given by $R = \lambda^2/l_a$ and therefore, the balance of capillary and dynamic pressures, σ/R and $\rho a l_a$, yields:

$$\sigma \frac{l_a}{\lambda^2} \sim \rho a l_a. \tag{3.3}$$

Thus, the wavelength λ is proportional to $(\sigma/\rho a)^{1/2}$. On the other hand, taking into account that the induced velocity v_a can be estimated as $v_a \sim \omega l_a$, as well as $v_a \sim (a l_a)^{1/2}$, the amplitude can be defined as $l_a \sim a/\omega^2$. Considering the ratio between these two fundamental scales in our work, l_a and λ, a fundamental non-dimensional number

$$G = \frac{l_a}{\lambda} = \left(\frac{\rho a^3}{\sigma \omega^4} \right)^{1/2}, \tag{3.4}$$

measures the relative amplitude of the capillary waves with respect to their wavelength. Depending on the values of G, the Reynolds number scales accordingly: i.e., given the expression of the Reynolds number in terms of the induced acceleration,

$$\mathrm{Re} = \frac{\rho \left(a L^3 \right)^{1/2}}{\mu}, \tag{3.5}$$

the length L should be either l_a or λ depending on whether G is smaller or larger than the unity, respectively (i.e., the smaller value of L between the two possibilities should be always taken). Consequently, for G smaller or larger than unity, $Re_{l_a} = (\rho a^2)/(\mu \omega^3)$ or $Re_\lambda = [(\rho \sigma^3)/(\mu^4 a)]^{1/4}$, respectively.

Figure 3.6 shows the ratio of the resulting bubble volume in the excited case over the unexcited case V_e/V as function of Re and G. Interestingly, for $G < 1$, where $\lambda < l_a$, one has that $V_e/V \simeq 1$, i.e. our experiments show that the acoustic excitation does not exert an appreciable effect on the ejected bubble size. Both angles are plotted together since contract angle are of second order variables with respect to G and Re.

However, for $G > 1$, numerical experiments show a dependency on Re as

$$V_e/V \simeq 1.9 - 0.65\mathrm{Re}. \tag{3.6}$$

Therefore, as one could expect, the system reflects a rather drastic behavior depending on the values of G around 1, providing a neat picture on the validity of this parameter to select the parametric regions of interest. In addition, our results show that the system collapses (no regular bubble emission occurs) for values of G over 100 approximately. As a result, for $1 < G \lesssim 100$ the system exhibits a quite simple dependency with Re alone, with a maximum value of V_e/V around 2 for vanishing Re. Last but not least, all cases tentatively explored for Re_λ values over 1.4 resulted in $V_e/V \simeq 1$ independently of G, where the surface tension limits the excitation effect.

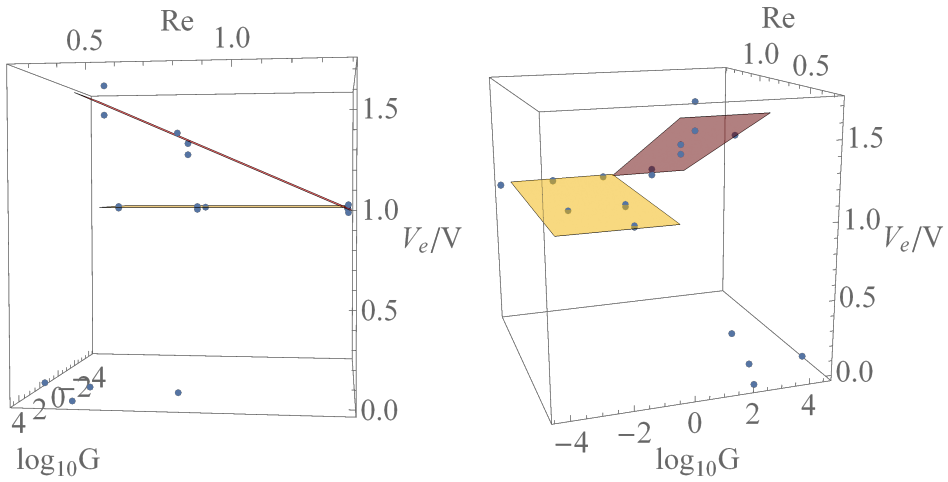

Figure 3.6: Three-dimensional plots of the bubble volume in the excited case over the unexcited case V_e/V as a function of the two dimensionless numbers: Re and G. Given that for G smaller than unity one always have $V_e/V \simeq 1$, we have used Re_λ values in the whole plot indistinctly.

3.5 Conclusions

In the present work, the formation of microbubbles in a microfluidic planar flow focusing configuration and its response to a lengthwise sinusoidal excitation is analyzed by means of full 3D numerical simulations. In the first place, the influence of the contact angle on the microbubble generation was studied. The contact angle treatment in numerical commercial software is still underdeveloped, turning out to the a fitting parameter with experimental work. The results showed a bubble volume change of $\sim 20\%$ when sweeping between a contact angle of 25° and 120°. In addition, the rectangular shape of the channel cross-section revealed two bubble size peaks when increasing the contact angle, corresponding to the moment in which the bubbles start touching the respective cross-section walls. The refinement of the mesh was likewise studied, confirming a similar physical behavior despite the level of refinement. The selection of a medium mesh element size of $0.74\,\mu$m on the cross-junction region achieved a trade-off between computational cost and reliable bubble characterization and 60° and 90° contact angle were selected, which best fitted the experimental observations.

The response of the system to the lengthwise sinusoidal vibration was characterized by a parametric exploration in excitation frequencies and accelerations for the two contact angles: 60° and 90°. A non-dimensional parameter $G = l_a/\lambda$ measures

the relative amplitude of the capillary waves l_a with respect to their wavelength λ and defines the Reynolds number accordingly (Re_λ, Re_{l_a}). Our experiments show that the generated bubbles are not appreciably affected by the acoustic excitation for values of G lower than the unity or $Re > 1.4$, corresponding to low amplitudes and/or high excitation frequencies. On the contrary, the effect of the excitation on the bubble volume for cases $G > 1$ exhibits a linear relation with Reynolds. Bubble volume increases with excitation amplitude, verifying previous experimental observations done by Chong et al (2015). The frequency is correlated with the highest amplitude that the system can absorb: the higher the frequency, the higher the amplitude limit. Above this amplitude, the system collapsed, which corresponds to values of G over 100 approximately. What is more, the collapse caused by numerical reason revealed in the present work the limit after which incompressibility conditions can no longer be imposed.

To conclude, this work also highlights that numerical simulations of acoustic excitations in 3D cross-junctions are extremely time-consuming, particularly for high frequencies. If the interface oscillation is to be perfectly captured, the need of a highly refined mesh makes the study even more expensive and time consuming. As a consequence, full 3D numerical simulations dealing with highly excited microfluidic devices are highly valuable but present several drawbacks in terms of required time.

References

Ajaev VS, Homsy G (2006) Modeling shapes and dynamics of confined bubbles. Annu Rev Fluid Mech 38:277–307

Bonn D, Eggers J, Indekeu J, Meunier J, Rolley E (2009) Wetting and spreading. Reviews of modern physics 81(2):739

Brackbill J, Kothe DB, Zemach C (1992) A continuum method for modeling surface tension. Journal of computational physics 100(2):335–354

Castro-Hernández E, van Hoeve W, Lohse D, Gordillo JM (2011) Microbubble generation in a co-flow device operated in a new regime. Lab on a Chip 11(12):2023–2029

Chen Y, Kulenovic R, Mertz R (2007) Numerical study on the formation of taylor bubbles in capillary tubes. In: ASME 2007 5th International Conference on Nanochannels, Microchannels, and Minichannels, American Society of Mechanical Engineers, pp 939–946

Chinnov E, Ron'shin F, Kabov OA (2016) Two-phase flow patterns in short horizontal rectangular microchannels. International Journal of Multiphase Flow 80:57–68

Chong ZZ, Tor SB, Loh NH, Wong TN, Gañán-Calvo AM, Tan SH, Nguyen NT (2015) Acoustofluidic control of bubble size in microfluidic flow-focusing configuration. Lab on a Chip 15(4):996–999

Chong ZZ, Tan SH, Gañán-Calvo AM, Tor SB, Loh NH, Nguyen NT (2016) Active droplet generation in microfluidics. Lab on a Chip 16(1):35–58

Cubaud T, Tatineni M, Zhong X, Ho CM (2005) Bubble dispenser in microfluidic devices. Physical Review E 72(3):037302

Dai L, Cai W, Xin F (2009) Numerical study on bubble formation of a gas-liquid flow in a t-junction microchannel. Chemical engineering & technology 32(12):1984–1991

Gañán-Calvo AM (1991) Oscillations of liquid captive rotating drops. Journal of fluid mechanics 226:63–89

Garstecki P, Gitlin I, DiLuzio W, Whitesides GM, Kumacheva E, Stone HA (2004) Formation of monodisperse bubbles in a microfluidic flow-focusing device. Applied Physics Letters 85(13):2649–2651

Gordillo JM, Gañán-Calvo AM, Pérez-Saborid M (2001) Monodisperse microbubbling: Absolute instabilities in coflowing gas–liquid jets. Physics of fluids 13(12):3839–3842

Herrada MA, Gañán-Calvo AM, López-Herrera JM (2011) Generation of small monodisperse bubbles in axisymmetric t-junction: the role of swirl. Physics of Fluids 23(7):072004

Herrada MA, Gañán-Calvo AM, Montanero JM (2013) Theoretical investigation of a technique to produce microbubbles by a microfluidic t junction. Physical Review E 88(3):033027

Herrada MA, Mohamed AS, Montanero JM, Gañán-Calvo AM (2015) Stability of a rivulet flowing in a microchannel. International Journal of Multiphase Flow 69:1–7

Martinez CJ (2009) Bubble generation in microfluidic devices. Bubble Science, Engineering & Technology 1(1-2):40–52

Plesset MS, Prosperetti A (1977) Bubble dynamics and cavitation. Annual review of fluid mechanics 9(1):145–185

Salari A, Dalton C (2015) Vibration effect on cross-flow and co-flow focusing mechanism for droplet generation. In: Microfluidics, BioMEMS, and Medical Microsystems XIII, International Society for Optics and Photonics, vol 9320, p 93201B

Santos R, Kawaji M (2010a) Effect of contact angle on gas slug formation, shape and flow in a microchannel t-junction by numerical simulation. In: 19th International Congress of Chemical and Process Engineering

Santos RM, Kawaji M (2010b) Numerical modeling and experimental investigation of gas–liquid slug formation in a microchannel t-junction. International Journal of Multiphase Flow 36(4):314–323

Santos RM, Kawaji M (2012) Developments on wetting effects in microfluidic slug flow. Chemical Engineering Communications 199(12):1626–1641

Vega EJ, Acero AJ, Montanero JM, Herrada MA, Gañán-Calvo AM (2014) Production of microbubbles from axisymmetric flow focusing in the jetting regime for moderate reynolds numbers. Physical Review E 89(6):063012

Wörner M (2012) Numerical modeling of multiphase flows in microfluidics and micro process engineering: a review of methods and applications. Microfluidics and nanofluidics 12(6):841–886

4

Acoustic excitation on cylindrical pinned microbubbles. Rapid microsensor to diagnose bacterial infection in COPD exacerbations *

The understanding of the dynamic acoustic response of a pinned microbubble represents the first step to the use of bubble shape modes as a diagnostic tool for complex fluids, such as saliva or sputum in Chronic Obstructive Pulmonary Diseases (COPD) clinical tests. Subject to an acoustic excitation with frequencies between 120 kHz and 320 kHz and amplitudes from 3 to 20 V, the bubble 3D oscillation is measured using a Digital Holographic Microscope (DHM). Bubble's vibration modes and resonance frequencies in the low-energy regime are characterized by means of a specifically developed unwrapping and mode recognition code. The liquid surface tension is related to the natural frequencies and estimated using them as fitting variables to the experiments. Damping is also calculated from the experimental data. The presence of harmonics and subharmonics is analyzed to ensure a linear regime.

*to be submitted as: Irene Arcos-Turmo, Álvaro Romero-Calvo, Guillaume Lajoinie, Elena Castro-Hernández, Michel Versluis, David Fernández-Rivas, "Acoustic excitation on cylindrical pinned microbubbles. Rapid microsensor to diagnose bacterial infection in COPD exacerbations". (2019)

4.1 Introduction

The use of crevices or artificial cavities on surfaces to control the microbubble location and its dynamic has enabled new applications in biology, like microswimmers (Bertin et al, 2015), cavitation for cleaning purposes (Verhaagen and Rivas, 2016) and microfluidics, such as the control of liquid motion, mixing, or streaming (Bolaños-Jiménez et al, 2017), to name a few. Vibration modes have been studied mostly theoretically (Plesset and Prosperetti, 1977) and for spherical bubbles (Versluis et al, 2010). Crevice bubbles subject to an acoustic streaming, highly dependent on the input energy, have however been lately investigated despite their broad application range (Gritsenko et al, 2018). On the one hand, bubbles respond in the low-energy regime with linear oscillations and no cavitation or pinch off occurs. The problem has been analytically studied by Gelderblom et al (2012) and Prosperetti (2012) in terms of frequencies, modes or pit dimensions dependence. Likewise, the steady streaming caused by the bubble interface oscillations has been experimentally analyzed (Wang et al, 2013; Bolaños-Jiménez et al, 2017). However, the few up-to-date available measuring methods for low bubble oscillations amplitudes and high excitation frequencies have so far limited their experimental research. The three-dimensional nature of the bubble oscillation and its size constitute a drawback for its visual imaging and tracing methods application too.

On the other hand, the use of higher energy inputs implies non-linear regimes, where oscillations become non-linear and cavitation or instabilities, such as parametric instabilities, can occur. Bubble shape modes can nonetheless throw a valuable information in high-energy regimes too. A considerable amount of experimental 3D mode studies have been reported for both spherical (Versluis et al, 2010) and pinned cylindrical bubbles (Wang et al, 2013). Versluis et al (2010) monitored the bubble shape using an integrated multi- high-speed camera (Brandaris, UTwente), giving an insight into the variability of modes depending on the bubble radius and driving pressure. Wang et al (2013) measured the bubbles oscillations using an inverted microscope and tracking particles, obtaining their shape modes and resonance frequencies using Fourier decomposition into cosines. The study of pinned microbubbles oscillations is not only restricted to their shape modes, but also to their possible harmonics and subharmonics, standing and traveling waves (Xu and Attinger, 2007) and, more recently, to their moving contact-line (Shklyaev and Straube, 2008; Xia and Steen, 2018).

The present research is focused on the experimental dynamic acoustic response of a pinned microbubble interface and the obtention of the liquid properties from this response. The shape modes and resonance frequencies of the bubble in the low-energy regime are characterized, where either parametric oscillations nor bubble ejections appear. To that purpose, similar configurations as those used by Bolaños-Jiménez et al (2017) were employed. One of the key novelties of the present project is the use of the

Digital Holographic Microscope (DHM), which can provide 3D-reconstructions of the bubble interface, as well as oscillation amplitudes in the range of nanometers. We aim to present information not achieved before: the direct experimental shape modes analysis of pinned microbubbles.

4.1.1 Application

Chronic Obstructive Pulmonary Disease (COPD) is a common preventable and treatable disease. Nonetheless, COPD is a leading source of morbidity and mortality worldwide. Periodic exacerbations, defined as an acute change in the baseline conditions that may warrant a change in regular medication, typically occur one to three times a year. Its cause is believed to be due to complex interactions between the host, bacteria, viruses, and environmental pollution, leading to an increase in the inflammatory load. In the literature, it is suggested that $50-70\,\%$ of exacerbations are due to respiratory infections (including bacteria, atypical organisms and respiratory viruses), $10\,\%$ are due to environmental pollution (depending on season and geographical placement), and up to $30\,\%$ are of unknown etiology (Sapey and Stockley, 2006). Therefore, a correct and fast diagnosis is crucial for a proper treatment to the patient, specially if antibiotics have to be administrated. Besides, the precise determination of when to use antibiotics is urgently needed worldwide for the reduction of costs, side effects and risks such as resistant bacteria.

However, no diagnosis method combines both reliability and fast-diagnosis. COPD generally results in an increase in the mucus' viscoelasticity, as well as coloration change. Accurate tests, such as sputum culture or resistances tests, require several days before detecting the presence of bacteria. Another procedure is to measure the mucus' macroviscosity with microrheometers. However, large discrepancies in sputum viscoelasticity measurements are found in patients with chronic bronchitis, ranging from $1\,\mathrm{Pa{\cdot}s}$ to $80\,\mathrm{Pa{\cdot}s}$ for viscosity at a constant shear rate of $0.4\,\mathrm{s}$ (Lai et al, 2009). Besides, these methods can modify sample properties, such as altering the molecular structure due to high shear stresses or requiring immersion of magnetic particles or fluorescent probes. The existing equipments lack portability, are mechanically and electronically complex, and consume considerable amounts of energy (rotating machinery, magnets, fluorescence probes, etc.). Cross-contamination risk between samples is not negligible; and a limitation shared by most techniques is the volume of sample to be analyzed ($> 20\,\mu\mathrm{l}$). All this results in subjective tests being more popular. They are also based on the same principles of color and viscosity variations, but are less time-consuming. Color is subjectively compared with Stockley's Chart (Stockley et al, 2000) and the viscoelastic properties changes are related to the mucus *purulence*, a confusing term used by doctors stretching the mucus sample with the fingers until it breaks. The filancemeter, a commercial device, requires well-calibrated samples with poor reproducibility (63% variation for small volumes $< 1\,\mu\mathrm{l}$ and $16\,\%$ for volumes

$< 5\,\mu$l) (Zahm et al, 1986). Thus, our final goal is to fabricate a novel acoustic and colorimetric microdevice to measure dynamic viscoelastic and color properties of small quantities of sputum ($< 15\,\mu$l), disposable, contact free, with a short diagnosis time and simple to understand. We strongly believe that a combinatorial analysis of color and viscoelastic properties of sputum represents an affordable and fast diagnosis tool. Thus, the first step is the study of the bubble modes and the extraction of rheological information from the dynamics of an acoustically excited pinned bubble in pure liquids. After that, complex fluids, both newtonian and non-newtonian, as well as the colorimetric measurements will be addressed. The objective is to combine a reliable colorimetric measurement with a novel acoustic concept: the correlation of the surface deformation patterns of a bubble inside sputum samples with the viscoelastic properties of healthy sputum: a concept not reported before.

4.2 Methods

4.2.1 Experimental Methods

Air bubbles are naturally entrapped in artificial crevices (or pits) patterned on silicon substrates by plasma dry-etching (Fernandez Rivas et al, 2010; Zijlstra et al, 2015). In this work, square shaped substrates (10 mm width, 500 μm thickness) containing cylindrical micromachined crevices of 50 μm diameter are used, in which the air is naturally entrapped when covered by a fluid. The pit is connected underneath to a pressurized air chamber, which enhances the control of the bubble curvature and pinning height by means of a hydrostatic pressure regulator.

The substrate is accommodated on a cylindrical glass holder with a cylindrical opening of 2 mm depth and 14 mm diameter. Once filled with ultra-purified water (Milli-Q), the container is covered with a thin cover glass (Lamelles couvre-objet Menzel-Gläser 100 μm thick) to avoid contamination and to ensure a constant volume of liquid. The holder is attached to a cylindrical piezoelectric transducer (Ferroperm, 5 mm thickness, 30 mm diameter), which acoustically actuates the system, see Figure 4.1.

A sinusoidal excitation was applied to the piezo using the stroboscopic unit of the Digital Holographic Microscope (DHM R1000 Lyncée Tec, SA) and an amplifier (Krohn-hite Corporation). Frequencies between 120 kHz and 320 kHz with 5 kHz steps, and voltages of 3, 5, 8, 10, and 20 V were studied. Four bubble periods were recorded at each frequency; the first of them was removed to suppress possible transient behaviors. Stroboscopic imaging was employed to study the bubble shape modes in steady state regime. Rectified mass diffusion contribution was neglected after running several preliminary tests due to the low-energy regime and negligible temperature and bubble volume changes.

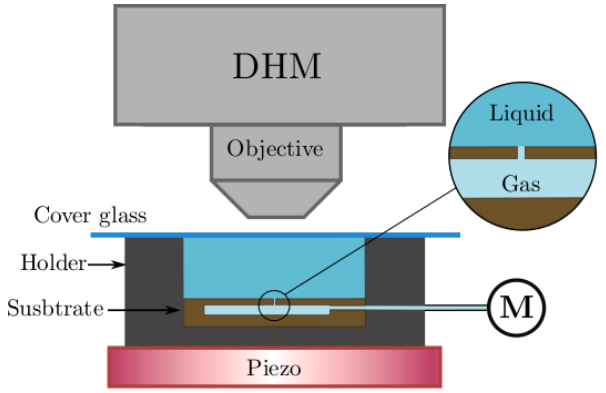

Figure 4.1: Experimental set-up scheme. The substrate is accommodated into a glass cylindrical holder and covered by a glass lamella after being filled. Pressure at the substrate chamber is controlled by a hydrostactic pressure regulator.

The DHM is a dynamic 3D typography equipment, consisting in two coherent 666-nm laser beams: a reference and an object beam. The object beam is diffused by the sample and interferes with the reference beam with a slight angle difference between their propagation directions. The interference results in an hologram, see Figure 4.3 in section 4.2.2, and is recorded by a CCD camera (Mikrontron EoSens 4CxP). A 63X microscope objective lens is employed. The wavefront deformation during the reflection by the sample, called dephasing, is measured with respect to a reference plane. Thus, the DHM measures the relative bubble's motion with respect to the substrate. By means of computational algorithms, both intensity and phase information are extracted. The phase image can provide a shape reconstruction of the sample. The extraction process is achieved by a commercial software (Koala, Lyncée Tec SA) and the reconstruction by a Matlab® code specifically developed for the present project (see section 4.2.2).

Despite the fixed DHM acoustic input to the transducer, which forces the excitation at a certain frequency and voltage, the final excitation delivered by the transducer does also depend on the piezo's resonance frequencies, employed liquids and rest of the component of the experimental setup. As a result, the linear to non-linear vibration boundary can not be prefixed at a specific voltage and the energy delivered to the bubble should be analyzed for each system. To this purpose, the piezo's voltage, intensity and phase were measured using a Digital Phosphor Oscilloscope (Tektronik DPO 4034), a voltage probe (Tek P6139A, 10Mohm) and a 5.6 Ω resistance (Zijlstra et al, 2015; Bolaños-Jiménez et al, 2017). The power was studied for the cases of 15 V and 20 V in water, and for 3, 5, and 8 V considering 20 % and 40 % glycerol solutions. Figure 4.2a displays the dimensionless power absorbed by the piezo versus

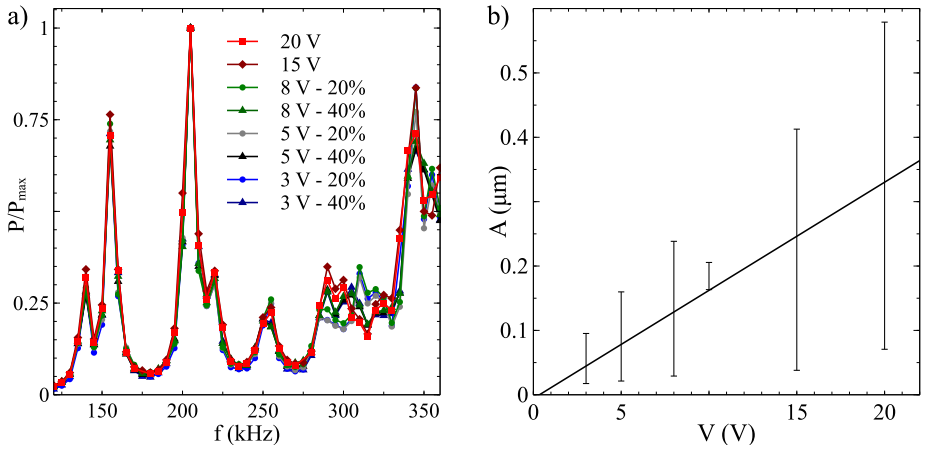

Figure 4.2: a) Power normalized with the maximum power for several cases varying voltage and viscosity; b) Average response amplitude of the bubble 25x25 central pixels versus applied voltage for a driving frequency of 170 kHz. Data corresponds to 3, 5, 8, 10, and 20 V in water and the solid line is a linear fit to the data ($R^2 = 0.436$).

the applied frequency. The piezo's response follows the same shape independently of the applied voltage. Although the power is highly dependent on the excitation frequency, no significant voltage variation within the studied frequencies was observed. However, the analysis is limited to one frequency sweep for each case. Figure 4.2b analyses the bubble response amplitude in water against voltage. A linear response cannot be ensured due to the low linear factor obtained when the response amplitude is linearized with respect to voltage. These results are in agreement with the dispersion later observed in the experimental data, see section 4.4. Further experiments are to be performed to confirm a linear excitation.

4.2.2 Analysis. Modal projection

To identify the presence of the different vibration modes, the bubble reconstruction is performed based on the extracted phase images. Holographic reconstruction methods are generally based on spacial unwrapping procedures. These procedures calculate the bubble interface with respect to a previously defined reference point, which is to be accommodated at the bubble's surrounding substrate. However, the bubble is not naturally pinned to the pit outer border in a perfect form, but might be irregularly pinned some millimeters inside the cavity due to its roughness. The difference in height between the substrate and the bubble contour because of its pinning or tilting made it necessary to generate an alternative procedure based on temporal unwrapping techniques, which does not experience such an strong dependence on

contour irregularities and border reflections. As a result, the experimental bubble is reconstructed for each experiment, not as a volumetric 3D reconstruction, but as an amplitude map, see Figure 4.3c. The latter is then projected on the different theoretical mode shape to obtain the modal coefficients. These operations, performed for each experiment, are listed in detail below:

1. Image preprocessing consisting on splitting the experimental files into the different frequencies and voltages, neglecting the first recorded period, and cropping the image to a square of side 2.2 times the radius of the pit, R, centered on the pit. The bubble contour recognition algorithm was improved and some cases were manually corrected (circular fitting of the pit border) to diminish the bubble's contour noise in the phase images.

2. Temporal unwrapping of each pixel signal, $p(t)$.

3. Subtraction of mean signal value to obtain the amplitude of the movement, $a(t)$.

$$a_t(t) = p(t) - \overline{p} \tag{4.1}$$

4. Fast Fourier transform (FFT) of each pixel $a_t(t)$.

5. Amplitude $a_m(f)$ and phase $p_m(f)$ selection of each pixel associated to a given frequency f.

6. Generation of the amplitude $A(x,y,f)$ and phase $P(x,y,f)$ matrix containing the entire image.

7. Filter absolute amplitude matrix noise with consecutive horizontal and vertical Hampel filters.

8. Generation of a real amplitude matrix by including the phase information through

$$A_{real}(x,y,f) = A(x,y,f) \cdot cos(P(x,y,f) - P_c(x,y,f)) \tag{4.2}$$

   where P_c is the phase at the center of the bubble. This temporary swift associates the maximum amplitude with the center of the bubble.

9. Generation of theoretical modes, as it will be seen bellow, equation 4.4. A theoretical amplitude matrix A_{theo} with the same size as the measured real amplitude matrix is generated.

10. Projection of the measured real amplitude matrix on the theoretical amplitude matrix for each mode. To take into account the lateral modes orientation, the projection is rotated to fit the theoretical mode orientation.

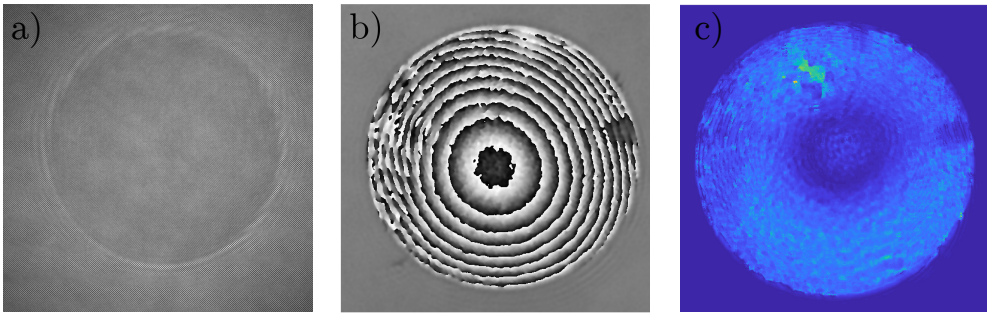

Figure 4.3: a) Hologram recorded by the DHM; b) Phase image reconstructed from the hologram; c) Amplitude map generated using our temporal unwrapping code.

4.3 Theory

The presence of each mode, i.e. the modal coefficient, is estimated with the wave equation on a circular simply-supported membrane problem, given by

$$\frac{\partial^2 h}{\partial r^2} + \frac{1}{r}\frac{\partial h}{\partial r} + \frac{1}{r^2}\frac{\partial^2 h}{\partial \theta^2} = \frac{1}{c^2}\frac{\partial^2 h}{\partial t^2}, \tag{4.3}$$

where $c = \sqrt{T/\rho_s}$, being T the membrane tension and ρ_s the mass per unit area of the membrane. Since the DHM only measures the movement relative to the substrate, just the modes response and not the motion as a rigid solid is observed. Assuming solutions of the form $h(r,\theta,t) = R(r)\Theta(\theta)e^{j\omega t}$ and applying separation of variables, one finally arrives to the following mode shape expression

$$h_{mn}(r,\theta,t) = J_m\left(f_{mn}\frac{r}{R}\right)cos(m\theta)cos(\omega_{mn}t), \tag{4.4}$$

where J_m is the m^{th} order Bessel function, R is the pit radius, f_{mn} is the spatial frequency of the mode m-n relative to the fundamental frequency f_{01} and ω_{mn} is the mode natural frequency. A selection of shape modes are represented in Figure 4.4. The movement of the bubble interface, $H(r,\theta,t)$, can be expressed as the modal superposition of the infinite modes given by the membrane problem (eq. 4.4),

$$H(r,\theta,t) = \sum_{m=0}^{\infty}\sum_{n=1}^{\infty} C_{mn}\cdot h_{mn}(r,\theta,t), \tag{4.5}$$

where C_{mn} are the modal coefficients (eigenvalues) and $h_{mn}(r,\theta,t)$ are the oscillation modes (eigenvectors).

The movement of the interface is now related to the experimental data, A_{real}, to obtain the modal coefficients for each mode. If we supposed the bubble to be

oscillating at a mode k-l, which implies a natural frequency ω_{kl}, the experimental real amplitude can be related to the previous theoretical interface movement as:

$$\begin{aligned} A_{real}(r,\theta)\cdot cos(\omega_{kl}t) &= H(r,\theta,t) \\ &= \sum_{m=0}^{\infty}\sum_{n=1}^{\infty} C_{mn}\cdot h_{mn}(r,\theta,t) \\ &= \sum_{m=0}^{\infty}\sum_{n=1}^{\infty} C_{mn}\cdot \tilde{h}_{mn}(r,\theta)\cdot cos(\omega_{mn}t) \end{aligned} \tag{4.6}$$

In order to calculate the coefficients C_{mn} at a given frequency, the orthogonality equation for two Bessel functions is employed, defined as

$$\int_0^1 sJ_p(as)J_l(bs)ds = 0 \text{ if } a \neq b \text{ or } p \neq l. \tag{4.7}$$

If this is applied to equation 4.6 multiplied by $r\tilde{h}_{kl}(r,\theta)$, only k-l modes are non-zero

$$\begin{aligned} P_{kl} &= \int_{r=0}^{R}\int_{\theta=0}^{2\pi} rA_{real}(r,\theta)\cdot\tilde{h}_{kl}(r,\theta)d\theta dr \\ &= \int_{r=0}^{R}\int_{\theta=0}^{2\pi} rC_{kl}\tilde{h}_{kl}(r,\theta)\cdot\tilde{h}_{kl}(r,\theta)d\theta dr. \end{aligned} \tag{4.8}$$

Taken into account that

$$\int_{r=0}^{R}\int_{\theta=0}^{2\pi} r\tilde{h}_{kl}(r,\theta)\cdot\tilde{h}_{kl}(r,\theta)d\theta dr = \frac{K}{2}\pi^2R^2J_k'(f_{kl})^2, \tag{4.9}$$

one finally arrives to the following expression for a general modal coefficient C_{mn} in cartesian coordinates,

$$C_{mn} = \frac{1}{\frac{K}{2}\pi^2R^2J_m'(f_{mn})^2}\int_{-R}^{R}\int_{-R}^{R} A_{real}(x,y)\cdot\hat{h}_{mn}(x,y)dxdy. \tag{4.10}$$

Once the presence of each mode is established, non-linear effects can be analyzed to ensure a linear response. In linear systems, a bubble interface responds to an external excitation vibrating at its fundamental frequency equal to the excitation frequency (neglecting damping). Nonetheless, non-linearities can arise, mainly due to an increase in the excitation amplitude. These non-linearities can be identified studying the presence of bubble's harmonics and subharmonics. As an example, the presence of subharmonics is a key feature in Faraday waves: parametric non-linear oscillations where surface waves vibrate at half the driving frequency due to oscillating gravitational or even pressure based perturbations. They can be defined by the

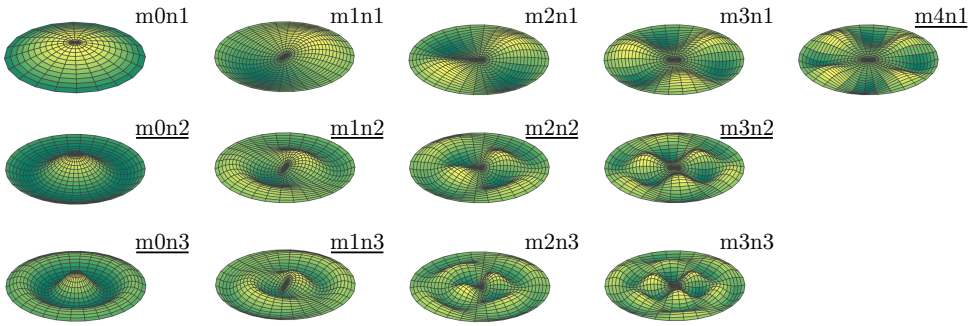

Figure 4.4: Pinned microbubble vibration modes obtained from the Bessel functions in the angular (m) and radial (n) directions and used for the modal coefficient projections. Underlined modes are the modes finally selected in the study.

Mathieu equation, a linearized Rayleigh-Plesset equation (Xu and Attinger, 2007). Parametric oscillations could also develop into the so called parametric instabilities. Another type of possible non-linearity is denoted by harmonics similar in strength to the fundamental. These non-linearities are more proper of quadratic terms in the Rayleigh-Plesset equation.

To obtain the surface tension from the bubble oscillation, a relation with the resonance frequencies is derived based on the dispersion relation and capillary waves properties. The bubble natural frequencies are given by the roots of the first kind Bessel function, j_{mn}, where the first axisymmetric roots are

$$j_{0n} = k_{0n}R = 2.405, 5.520, 8.654, 11.792, 14.931, \tag{4.11}$$

being R the radius of the membrane and k the wavenumber. The wavenumber is related with the natural frequencies ω_{mn} by the wave velocity as $c = \omega_{mn}/k_{mn}$ for each particular mode. Thus,

$$\omega_{mn} = k_{mn} \cdot c = j_{mn}/R \cdot c. \tag{4.12}$$

Considering the capillary wave solution, the frequency can also be defined as

$$\omega_{mn} = \sqrt{|k_{mn}^3|\sigma/\rho}, \tag{4.13}$$

where ρ is the liquid density and σ the surface tension. Combining equations 4.12 and 4.13, the surface tension results in

$$\sigma = \rho\, \omega_{mn}^2\, (R/j_{mn})^3. \tag{4.14}$$

Likewise, the wave velocity results in

$$c = \omega_{mn}\, (R/j_{mn}). \tag{4.15}$$

	m0n2	m0n3	m1n2	m1n3	m2n2	m3n2	m4n1
$\xi = 0$	140.26	275.31	200.96	350.93	264.10	329.80	226.06
$\xi = 0.15$	138.67	272.19	198.69	346.96	261.11	326.07	223.51
3 V	131.59	204.52	173.01	250	160	280	140
5 V	132.54	205.29	189.75	330	160	295	180
8 V	132.91	207.97	189.59	325	165	265	225

Table 4.1: Theoretical natural frequencies between 120 kHz and 320 kHz considering a system without damping and with a damping factor of $\xi = 0.15$, together with the measured experimental resonance frequencies.

Thus, a relation between the surface tension and the natural frequencies is deduced. For comparison, the theoretical frequencies were later on estimated based on the surface tension of water.

Last, the liquid viscosity can be obtained from the bubble damping factor, which is related to the different peak's bandwidths. The damping coefficient, ξ, is estimated using the Half-Power method as

$$\xi = \Delta f / 2f. \tag{4.16}$$

4.4 Results and discussion

Once the bubble reconstruction was completed, the projection on the theoretical natural frequencies was performed. The resulting axisymmetric and non-axisymmetric modes presence for the different voltages is summarized in Figure 4.5. This modes presence corresponds to the modal coefficients, C_{mn}, normalized with the average modal coefficient of modes m0n4 to m0n6 for each voltage, denoted as B. Modes with natural frequencies between 120 kHz and 360 kHz were considered, i.e. m0n2, m0n3, m1n2, m1n3, m2n1, m2n2, m3n1, m3n2, and m4n1 (see Figure 4.4). Modes m2n1 and m3n1 were then discarded due to their low modal coefficients. A fit to the experimental data of the form $f(x) = a\,e^{-(\frac{x-b}{c})^2} + d$ was performed as an approximation to the experimental resonance curves for the first three modes. The fit was employed to obtain the resonance frequencies for the three first modes, whereas the frequency corresponding to the highest coefficient was selected for the rest of modes. The resulting resonance frequencies are given in Table 4.1.

The modal coefficients for non-axisymmetric modes (m1n2, m1n3, m2n2, m3n2 and m4n1) are lower than those for axisymmetric modes (m0n2 and m0n3), but not small enough to be neglected. In theory, a perfectly simply-supported membrane subject to perpendicular forces is limited to axisymmetric modes. Nonetheless, the

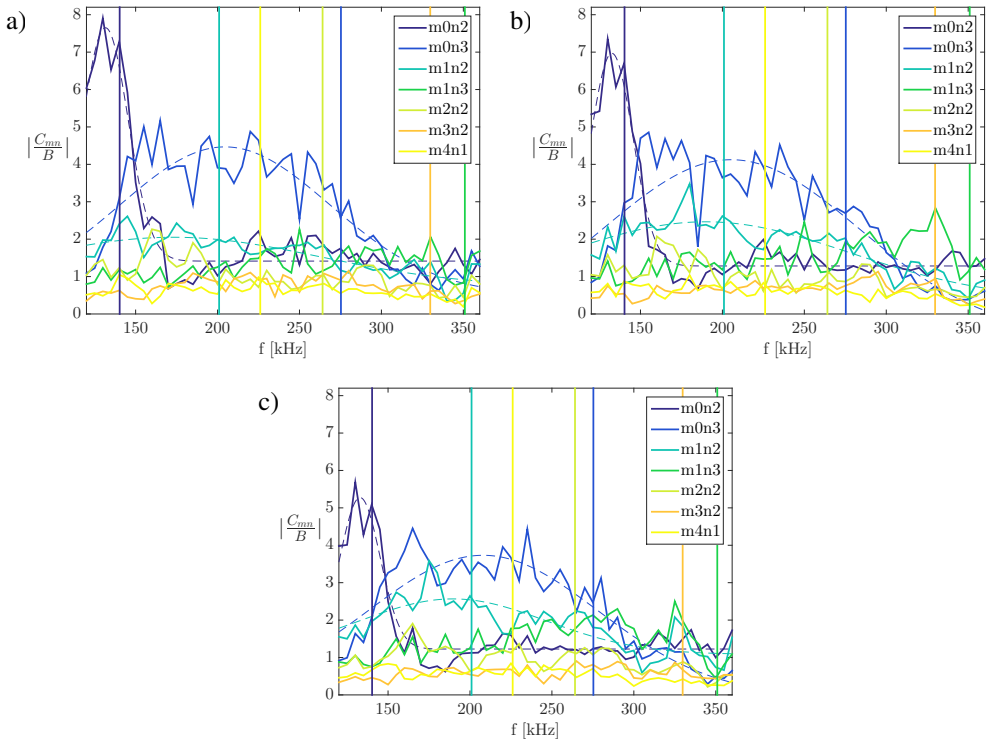

Figure 4.5: Dimensionless mode presence for a) 3 V, b) 5 V, and c) 8 V experiments against the excitation frequency for axisymmetric and non-axisymmetric modes. Vertical lines correspond to theoretical natural frequencies for $\xi = 0$ and $\sigma = 0.072$ N/m. Dotted lines are the fittings of the form $f(x) = a\,e^{-(\frac{x-b}{c})^2} + d$.

presence of lateral perturbations, bubble lateral tilting, irregular pinning, and surface instabilities, proper of experimental conditions, hypothesized to be responsible for the existence of these lateral modes. As a matter of fact, the bubble tilting was measured; the bubble peak for each frame was located, computed its mean distance to the pit center along each case. A mean center displacement value of $4\,\mu$m, with respect to the $50\,\mu$m pit diameter was found, which denotes a not negligible tilting. On the other hand, an average damping coefficient between 0.09 and 0.3 was estimated from the first two considered modes (m0n2, m0n3) and a value of $\xi = 0.15$ was selected for comparison. Theoretical natural frequencies with and without damping were then calculated based on the derived surface tension expression for water ($\sigma = 0.072\,$N/m) and are comprised in Table 4.1. A general shift between the theoretical and the experimental resonance frequencies is observed; the surface tension expression seems to slightly overestimate the theoretical frequencies. Other approaches, as the thin clamped circular membrane done by Gritsenko et al (2018), also lead to theoretical frequencies higher than our measured experimental frequencies.

Figure 4.6 displays the presence of harmonics and subharmonics against the excitation frequency for a wider range of analyzed frequencies. Here, the modal coefficients of each mode were normalized with the average modal coefficient on that excitation frequency for each voltage and mode. No significant harmonics were found, which evidences the lack of non-linearities and reinforces the low-energy regime assumption. The surface tension was then estimated from the first three studied modes using the theoretical natural frequencies as fitting variables to the experimental resonance frequencies, resulting in an average surface tension of $\sigma = 0.0549\,$N/m (without damping); modes m0n2 and m1n2 showed the best agreement with $\sigma = 0.0639\,$N/m and $\sigma = 0.0607\,$N/m, respectively. These values are in agreement with the previous overestimation of the theoretical frequencies. Although considerable efforts have been done until the moment, specially for the generation of the temporal unwrapping and mode recognition code, these are however provisional results. The measured data is being treated to further reduce the modal presence dispersion, which current mean value for mode m0n2 is 2.516, and which linearly decreases to 0.511 for mode m4n1. A proportional relation between more relevant modes and dispersion has been observed but it is however still large to draw final conclusions.

The current discrepancies may be the result of experimental dispersion, data treatment or due to the theoretical approach. Further experiments are to be performed to complete the data for 10, 15, and 20 V, as well as broaden them to 20 % and 40 % glycerol solutions and even higher voltages, since non-linearities have not been observed yet. Although peak location refinements, Hampel filters and normalization has been applied, further data refinements are to be implemented. As explained earlier, bubbles in artificial crevices typically show convex curved interfaces that may vary with the pinning. Therefore, the comparison with plain models might be unfair in

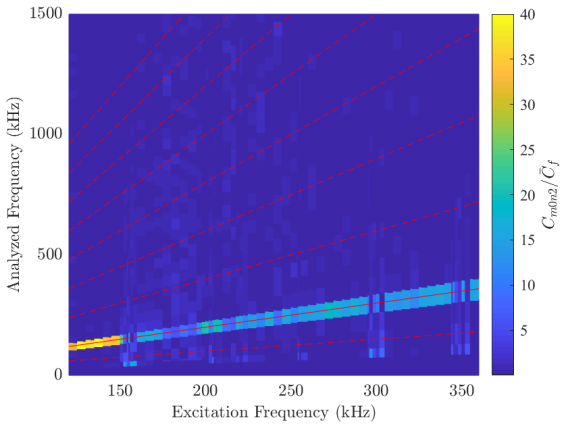

Figure 4.6: Dimensionless mode presence against the excitation and the analyzed frequency, for mode m0n2 and 5000 mV. The red continuous line is the excitation frequency and red dotted lines correspond to subharmonics and harmonics.

some of the cases. Likewise, the pinning could create a boundary condition closer to a clamped rather than to a simply-supported boundary conditions. Lastly, the dispersion may also arise from the DHM working conditions, highly dependent on the settings due to its high sensitivity, which could for instance degenerate into camera electronic noise. This has also been considered, as the present experiments were the first to be performed on a new DHM.

4.5 Conclusions and future developments

The dynamic acoustic response of a pinned microbubble in the low-energy regime is being studied using the Digital Holographic Microscope (DHM) for several amplitudes in the range of 120 kHz to 320 kHz. A temporal unwrapping Matlab® code, which transforms the DHM intensity and phase images into a bubble amplitude map, as well as the extraction of the modal coefficients, has been developed. Resonance frequencies of the modes contained in the studied frequency range were identified and the contribution of harmonics and subharmonics dismissed. Applied voltages were proved to maintain the system in the low-energy or linear regime. So as to associate the bubble oscillation to the liquid properties, a relation between the surface tension and the resonance frequencies was derived based on capillary waves properties, resulting in a surface tension of $\sigma = 0.0549$ N/m. The resulting theoretical frequencies were also slightly overestimated. These discrepancies could arise from experimental dispersion, data treatment or the theoretical approach. Further data refinements are currently being performed to reduce the experimental dispersion and thus, the exposed

results are to be considered provisional yet.

Despite the differences, the present approach constitutes a simple and straight forward procedure for calculating pinned bubble's theoretical frequencies and a method to measure and identify mode shapes, resonance frequencies and, above all, liquid properties, such as the surface tension. It is a first step to the use of bubble forced oscillations as a diagnostic tool for complex fluids characterization, such as saliva or sputum in COPD clinical tests.

Future work will focus on the acquisition of other liquid properties, such as viscosity, and will also aim to understand the possible disagreement between theoretical and experimental resonant frequencies. Forthcoming developments will contemplate other pits designs in order to reduce wall reflections and to achieve a most stable and regular pinning, also enhancing the bubble curvature control. Tilted-walls or cryro fabricated pits are possible considered designs.

References

Bertin N, Spelman TA, Stephan O, Gredy L, Bouriau M, Lauga E, Marmottant P (2015) Propulsion of bubble-based acoustic microswimmers. Physical Review Applied 4(6):064012

Bolaños-Jiménez R, Rossi M, Rivas DF, Kähler CJ, Marin A (2017) Streaming flow by oscillating bubbles: quantitative diagnostics via particle tracking velocimetry. Journal of fluid mechanics 820:529–548

Fernandez Rivas D, Prosperetti A, Zijlstra AG, Lohse D, Gardeniers HJ (2010) Efficient sonochemistry through microbubbles generated with micromachined surfaces. Angewandte Chemie International Edition 49(50):9699–9701

Gelderblom H, Zijlstra AG, van Wijngaarden L, Prosperetti A (2012) Oscillations of a gas pocket on a liquid-covered solid surface. Physics of fluids 24(12):122101

Gritsenko D, Lin Y, Hovorka V, Zhang Z, Ahmadianyazdi A, Xu J (2018) Vibrational modes prediction for water-air bubbles trapped in circular microcavities. Physics of Fluids 30(8):082001

Lai SK, Wang YY, Wirtz D, Hanes J (2009) Micro-and macrorheology of mucus. Advanced drug delivery reviews 61(2):86–100

Plesset MS, Prosperetti A (1977) Bubble dynamics and cavitation. Annual review of fluid mechanics 9(1):145–185

Prosperetti A (2012) Linear oscillations of constrained drops, bubbles, and plane liquid surfaces. Physics of fluids 24(3):032109

Sapey E, Stockley RA (2006) Copd exacerbations· 2: Aetiology. Thorax 61(3):250–258

Shklyaev S, Straube AV (2008) Linear oscillations of a compressible hemispherical bubble on a solid substrate. Physics of Fluids 20(5):052102

Stockley RA, O'Brien C, Pye A, Hill SL (2000) Relationship of sputum color to nature and outpatient management of acute exacerbations of copd. Chest 117(6):1638–1645

Verhaagen B, Rivas DF (2016) Measuring cavitation and its cleaning effect. Ultrasonics sonochemistry 29:619–628

Versluis M, Goertz DE, Palanchon P, Heitman IL, van der Meer SM, Dollet B, De Jong N, Lohse D (2010) Microbubble shape oscillations excited through ultrasonic parametric driving. Physical review E 82(2):026321

Wang C, Rallabandi B, Hilgenfeldt S (2013) Frequency dependence and frequency control of microbubble streaming flows. Physics of Fluids 25(2):022002

Xia Y, Steen PH (2018) Moving contact-line mobility measured. Journal of Fluid Mechanics 841:767–783

Xu J, Attinger D (2007) Acoustic excitation of superharmonic capillary waves on a meniscus in a planar microgeometry. Physics of Fluids 19(10):108107

Zahm J, Puchelle E, Duvivier C, Didelon J (1986) Spinability of respiratory mucous. validation of a new apparatus: the filancemeter. Bulletin europeen de physiopathologie respiratoire 22(6):609–613

Zijlstra A, Rivas DF, Gardeniers HJ, Versluis M, Lohse D (2015) Enhancing acoustic cavitation using artificial crevice bubbles. Ultrasonics 56:512–523

5 Conclusions

The present thesis is a compilation of three studies in the field of microfluidics, more concretely, the generation of microbubbles and the effect that different applied forces have on them.

A microbubble generation state of the art in terms of applications, employed fluids, working regimes and microfluidic devices is introduced in the first place. Several microfluidic devices: cross-junction, T-Junction, planar and axisymmetric flow focusing are compared with regard to their operational woking regime -bubbling, jetting or squeezing- and achievable microbubble size, as well as their fundamental advantages and limitations.

In the second chapter, a novel swirl flow-focusing microfluidic axisymmetric device for the generation of monodisperse microbubbles at high production rates is presented. By forcing a swirl effect on the liquid stream, a more stable production, as well as a microbubble size reduction -up to 57% compared to the axisymmetric flow focusing-, is achieved due to the enhanced gas meniscus stability. The swirl is shown to expand the bounds of the jetting regime, inhibiting the bubbling regime. An experimental study is performed for various blade angles -0°, 40°, 60°, and 80°- and numerous gas to liquid flow rate ratios; validating previous numerical simulations and the previous flow focusing scaling law proposed by Gañán-Calvo [Gañán-Calvo, *Physical Review E*, 2004, 69(2), 027301]. Chips with 60° blades exhibit the best combination of swirl effect and robustness against perturbations.

Chapter three is devoted to the active control of microbubble size on planar flow focusing devices by means of an acoustic streaming or mechanical excitation. Few numerical studies have been reported so far, despite the invaluable information that computational analysis can through on this topic. In this chapter, the microbubble generation is numerically analyzed for an ample range of acoustic accelerations and frequencies and for several contact angles. A bubble volume change of $\sim 20\%$ when sweeping the contact angle between 25° and 120° was observed. The addition of an acoustic excitation showed a correlation between the frequency and the highest amplitude that the system can absorb without collapsing. Likewise, bubble size increases with the excitation amplitude. A theoretical framework for the physics and parametric description of that tuning is also presented.

Finally, the effect of an acoustic excitation, not on bubble generation, but on a pinned microbubble in the low-energy regime is experimentally analyzed. Here, the goal is not to modify the bubble size, but to characterize liquid properties based on the bubble oscillation for medical diagnosis application. The novel Digital Holographic Microscope (DHM) was used for measuring the bubble interface movement and an unwrapping and mode recognition code is specifically developed for this chapter. Modes shapes and resonance frequencies were identified and related to the liquid surface tension to obtain an approximation to the surface tension. The existence of harmonics and subharmonics were analyzed to confirm a linear regime. Further noise-reduction procedures as well as a viscosity relation to the bubble oscillation are to be further developed.

Acknowledgements

This thesis is the result of a research project carried out at the Dpto. de Ingeniería Aeroespacial y Mecánica de Fluidos of Escuela Técnica Superior de Ingenieros at Universidad de Sevilla, Spain. The financial support for this project was provided by the Ministry of Economy and Competitiveness of Spain. I gratefully acknowledge its support.

I am grateful to Professor Gañán-Calvo, who gave me the opportunity to join his research group and has always believed in me.

I thank Associate Professor Castro-Hernández, for accepting this challenge and making it her own project too. For her constant support and sincere advice, especially during the last two years, and for being the catalyst for my research stay at University of Twente. She has shown me what it means to work in a scientific team, independently of the possible problems that could arise.

I also owe a debt of gratitude towards Assistant Professor Fernández-Rivas for his continuous help, his tireless spirit and energetic discussions. He revealed me how science can help people, how our work can have a direct impact in society, how close results can be from their applications if you believe in them. Many thanks also to Professor Versluis and Guillaume Lajoinie for welcoming me to PoF and for the fruitful discussions and useful feedback. I certainly learnt a lot at UT those four months. I would like to recognize S.Schlautmann (Clean room microfabrication) for his technical support and the rest of PoF and MCS group members for their valuable discussions, help and time spent together.

A special thanks goes to my department colleagues (both aeronautics and fluid mechanics), for sharing this period together, for both personal and scientific discussions, coffee breaks and lunchtimes. I would like to thanks Bea, Dory, Manolo and Jorge for their technical support; you made the present thesis run smoothly along these years. To my office and PhD mates during these last years: Alonso, Eulalia and Julio; we have spent a nice time together, both inside and outside university. A very special gratitude goes to Paco Cruz, my PhD colleague; you have always encouraged me and I truly hope you find your way in science as you dreamt it. I would also like to thank

Ingeniatrics employees, who helped me with my projects. This section could not be finished without mentioning my new “brother”, Álvaro Romero. Thanks for your invaluable help in chapter 4, your spirit, the laughs and, of course, good luck in the United States! (try not to handle too many projects simultaneously).

Last but not least, an invaluable gratitude goes to those who supported me from the beginning and even in the difficult moments: my family and Alfonso Valenzuela. To my friends, specially to María Márquez, who has always listened to me and cheered me up.

And for those who know me well, I thank God above all, for the possibility of finishing this PhD, for guiding and accompaning me in every moment of my life, for being my strength and happiness.

...and to the thesis itself. It has had its lights and shadows,
but I have learnt, matured and become what I am!

About the author

Irene Arcos-Turmo was born the 3rd October 1990 in Sevilla, Spain. She studied Industrial/Mechanical Engineering at Universidad de Sevilla, where she got her bachelor-master degree in 2013 with the thesis "Nebulización Flow Blurring a altas viscosidades", under the supervision of Prof. Gañán-Calvo. She moved to Sweden, where she got a Mechanical Engineering Solid Mechanics master degree in 2014 by the Royal Institute of Technology (KTH), Stockholm. Her master thesis took place close to Zürich, Switzerland, at the Dr.Müller AG company with the title: "Fundamix® Vibromixer". She started then her PhD at Universidad de Sevilla under the supervision of Prof. Gañán-Calvo and Associate Prof. Elena Castro-Hernández as part of the national project from the Spanish Ministry of Economy, Industry and Competitiveness under the grant DPI2016-78887.